J. Appl. Comput. Mech., 12(3) (2026) 848-865
DOI: 10.22055/jacm.2025.48499.5278

ISSN: 2383-4536
jacm.scu.ac.ir

Shahid Chamran University of Ahvaz

Journal of Applied and Computational Mechanics

Research Paper

Finite Element Analysis of MHD Thermal Management in a Ventilated Cavity with Dual Obstacles Using Advanced Ternary Hybrid Nanofluids

Amanullah Phulpoto[1], Abid A. Memon[1], M. Asif Memon[1,2,3], KaviKumar Jacob[2], Mustafoyev Komiljon[3]

[1] Department of Mathematics, Basic Sciences and Humanities, Sukkur IBA University, Sukkur, 65200, Sindh, Pakistan,
Email: amanullah@iba-suk.edu.pk (A.P.); abid.ali@iba-suk.edu.pk (A.A.M.); asif-memon@iba-suk.edu.pk (M.A.M.)

[2] Department of Mathematics and Statistics, Faculty of Applied Sciences and Technology, Universiti Tun Hussein Onn Malaysia, Pagoh Campus, 84600 Pagoh, Malaysia, Email: kavi@uthm.edu.my (K.J.)

[3] Center for Research and Innovation, Asia International University, Bukhara 200100, Uzbekistan, Email: k.mustafoyev@oxu.uz (M.K.)

Received June 02 2025; Revised October 08 2025; Accepted for publication October 09 2025.
Corresponding author: M. Asif Memon (asif-memon@iba-suk.edu.pk)

Abstract. Thermal management of ventilated cavities is one of the most significant challenges in the design of microfluidic heat sinks, electronic cooling systems, and medical diagnostics systems. The objective of this study is to examine the thermal and fluid dynamic response of a ventilated cavity with two heated obstacles under the influence of an external electromagnetic field. The ventilated cavity is filled with advanced ternary hybrid nanofluids (THNF) that account for the shape, volume and enhanced thermal properties of the nanoparticles. The governing continuity, Navier–Stokes & energy equations were solved numerically using the Finite Element Method (FEM) in COMSOL Multiphysics 6.2. This study considered six parameters: Reynolds number (*Re*), Hartmann number (*Ha*), magnetic field angle, particle shape factor ((*n* = 3.7 (cylindrical shape), 5.7 (Brick shape) and 4.9 (Platelets)), obstacle-gaps, and nanoparticle volume fractions. The findings show that increasing *Re* and increasing volume fractions increase heat transfer, whereas increasing *Ha* decreases the velocity and thermal transport characteristics of the fluid. A magnetic field angle of 90° was shown to enhance heat transfer at specific points in the cavity, with overall reductions in buoyancy flow and heat transport. The study identified the optimal condition for minimum entropy generation of (5.64×10^{-4}) occurred at *Re* = 2000, *Ha* = 25, and ϕ = 1%, and result for effective thermal insulation (minimum average Nusselt number = 17.677), occurred at *Re* = 100, *Ha* = 50 and ϕ = 10%.

Keywords: Ternary Hybrid Nanofluids (THNF), Ventilated Cavity, Dual Obstacles, Magnetohydrodynamics (MHD), Entropy generation.

1. Introduction

This Heat transfer analysis in cavities and channels, particularly those incorporating obstacles of various shapes, attracts significant research interest due to their numerous applications and complex fluid-thermal interactions. Among these, the study of convective heat transfer in ventilated cavities has gathered special attention for its simplicity and vital applications in engineering science. Over the past decade, convection and conduction problems within cavity channels, especially with the introduction of obstacles, have gained paramount importance due to the resistance created in the fluid flow.

Thermal management in cavities containing hot obstacles offers numerous interesting applications. This supports the use of this phenomenon in diverse fields, including thermal management with stationary obstacles, rotary flow applications, air conditioning maintenance, oil drilling operations, cooling components, heat engines, solar collectors, and food processing in industries. In each of these phenomena, it is necessary to update thermal management systems and understand fluid particle flow behavior for optimizing performance. By analyzing each of these phenomena, scientists and designers can recommend impactful solutions and provide better functionality for these applications [1].

To optimize heat transfer in a ventilated cavity, it is common practice to introduce solid obstacles inside, which redirects the velocity flow within the cavity and consequently enhances heat transfer. These obstacles can facilitate more uniform flow patterns and improve heat exchange from the fluid to the channel surroundings.

The study by Priam et al. [1] numerically examined 2D mixed convection in a vented square cavity with a rotating heated cylinder. The study used FEM to examine fluid flow and heat transfer by adjusting Re and Gr numbers. Complex flow and thermal characteristics were revealed by key quantitative findings, such as the dependence of heat transfer on Re, Gr cylinder position, and

Published online: October 12 2025

rotation direction. Natural convection from a finned horizontal cylinder was numerically optimized in a previous study conducted by Abu-Hijleh [2]. By optimizing obstacle number, size, and location, it minimized entropy generation and maximized the Nusselt number. Appropriate obstacle placement was found to significantly reduce entropy generation and heat transfer. Heat transfer with MHD and THNF flow in a square cavity with hot obstacles were numerically studied by Abraham et al. [3]. A high Re and volume fraction increased heat transfer rate, whereas a high Ha generally decreased it, according to the study's successful quantification of the effects of six parameters. Additionally, the ideal values for the minimum Nusselt number and minimum entropy generation were determined.

Transverse mixed convection in a vented enclosure with a heated bottom wall was numerically examined in the work by Saha et al. [4]. The governing equations for airflow (Re (50-1000), Ri (0-10)) were resolved by the two-dimensional model using the finite element method. The findings demonstrated that the locations of the inlets and outlets considerably changed the temperature fields and heat transfer across heated walls. For the Nusselt number, an empirical correlation was created. Separately, Joodi et al. [5] modeled flocculation basin turbulence in their study. Turbulence increased with increasing obstacle length, while turbulent kinetic energy decreased with increasing obstacle thickness. More turbulence was produced by semi-circular tips than by rectangular ones. Changes in inlet velocity had a significant impact on particle collision rates and turbulence. In a study by Radhakrishnan et al. [6], mixed convection from a heat-generating element in a vented cavity with or without obstacles was examined. The ideal obstacle heights and locations for improving heat transfer were determined using numerical techniques. These results were confirmed by experiments, which demonstrated that correlations established for the maximum dimensionless temperature and average Nusselt number agreed well with numerical results.

In a different numerical study by Nougbléga et al. [7], mixed convection of air in vented cavity with the obstacle was examined. It examined flow and thermal fields using finite differences for Reynolds numbers (10–200) and Rayleigh numbers 10^4 –10^6. The findings demonstrated that obstacle placements produced heated and isolated zones, offering a comparative framework for intricate cavity heat transfer. Natural convection in a magnetized staggered cavity containing Al_2O_3 nanoparticles was numerically investigated by [8]. It was discovered that raising the Ha increased the Bejan number while lowering the average Nusselt number. While flow strength was higher at smaller Rayleigh numbers, velocity was greatly increased by larger nanoparticles. The study by Aun et al. [9] experimentally and numerically investigated natural and forced convection in an enclosure with a heated block and obstacles.

Varying obstacle configurations and heat fluxes (240–1425 W/m^2) were explored. Results showed partially cut obstacles enhanced heat transfer by ~30% and reduced block temperature by ~11% compared to plain blocks at specific conditions (Re = 0, q = 240 W/m^2). The study by Hamzah et al. [10] examined transient mixed convection in a vented enclosure featuring a cylinder and a flexible obstacle. It investigated Richardson, Cauchy, and Re using FEM. Flexible obstacles produced better average Nusselt numbers, according to the results. The average Nusselt number increased by up to 59% at Ri = 200 when Re was raised from 50 to 250.

Non-Newtonian fluid convection in an obstacle square cavity was examined both experimentally and numerically in the work by Rehman et al. [11]. Increased Richardson number augmented average heat transfer was demonstrated by finite element analysis, which covered power law indices (0.5, 1.0, 1.5) and obstacle gaps (0.2-0.6). Heat flow was also accelerated by wider obstacle gaps. The work by Kefayati [12] used FDLBM to analyze laminar mixed convection of non-Newtonian (shear-thinning) alumina nanofluids in a lid-driven cavity. According to the results, heat transfer decreased as the Richardson number increased and the power-law index decreased (n = 0.2–1). Heat transfer was enhanced by nanoparticle addition (up to ϕ = 0.09), with the biggest impact at n = 0.2. In the work done by Mahmoudiet al. [13], mixed convection of a copper-water nanofluid in a vented square cavity (Re = 50-1000, Ri = 0-10, ϕ = 0-0.05) was numerically examined. It looked into the effects of heat sources and four different inlet/outlet configurations. The average Nusselt number, streamlines, and isotherms were displayed in the results, and the algorithm validation showed good agreement.

Using FEM, the study by Bellahcene et al. [14] numerically examined the forced convective heat transfer of Al_2O_3 nanofluids in (STHE). They discovered that as the inlet velocity and volume fraction increased, so did the heat transfer. For ϕ = 3%, the friction factor rose by up to 26.72%, while Nusselt numbers increased by up to 7.62%. Mixed convection in a horizontal channel with alternating obstacles and an external magnetic field was numerically investigated by Ali et al. [15]. Obstacle height and orientation were found to modulate flow and heat transfer using FEM. As the Re increased, fluid motion accelerated; however, as the concentration of nanoparticles and magnetic strength increased, fluid motion decreased. At Ha = 50, heat transfer augmentation was 22.14% lower than at Ha = 0, but 5% nanofluid demonstrated 33.86% greater heat transfer than base fluid.

The study by Biswas et al. [16] examined the use of flow injection to enhance mixed convection in a grooved channel. Researchers methodically examined injection parameters, Re (50–200), and Richardson number (0.1–10) using an internal CFD code. According to the results, injection was consistently better, achieving a notable improvement in heat transfer that varied from 50% to 218% depending on the circumstances. In the work by Biswas [17], segmental and whole heating were used to numerically examine mixed convection in a ventilated enclosure. Vertical walls (bottom, middle, and top) supported the heater segments. The performance of Re (50–200) and Ri (0.01–100) was examined. Heat transfer was improved through bi-segmental heating; the best places depended on Re and Ri, and the improvement increased as the number of segments increased. In the work by Biswas et al. [18], BFDM was used to numerically analyze heat transfer and pumping power in a bottom-heated porous cavity with Cu-water nanofluid. Re (10-200), Ri (0.1-20), Da (10^{-7}-10^{-4}), ε (0.1-1), ϕ (1-5%), and aspect ratio (0.25-2) were among the parameters. The findings demonstrated the impact of parameters on heat transport and observed a notable increase in pumping power when Re rose above 100 or Da fell below 10^{-5}. Conjugate natural convection of an Al_2O_3-water nanofluid in a differentially heated enclosure with an inclined obstacle was numerically examined by Barik et al. [19] using COMSOL. Heat transfer was improved by convection, which predominated at high Rayleigh numbers ($\geq 10^6$). When the obstacle angle was $30 < \emptyset \leq 60$, the average Nusselt number peaked. Between $\emptyset$ = 90°and $\emptyset$ = 30°, there was an improvement in Nu of roughly 7%.

Mixed convection of non-Newtonian power-law fluids (n = 0.6–1.4, Re = 10^4) in a lid-driven cavity with a heated triangular obstacle was numerically investigated by Kumar et al. [20]. Aspect ratio (0.25–0.75), Pr (1–100), and Ri (0.1–10) were among the parameters that were examined. The findings indicated that flow dispersion increased with increasing aspect ratio and that heat transfer was enhanced at aspect ratio 0.25. The flow of a magnetized ferric oxide–water nanofluid in a fillet square cavity with a rotating heated cylinder was numerically examined by Rehman et al. [21], taking entropy generation into account. The effects of volume fraction (0-0.05), angular velocity (0-5), and Ha (0-100) were investigated using GFEM. The findings indicated that while viscous and thermal entropy decreased, Nusselt number increased as volume fraction and angular velocity increased. The study by Mahmood et al. [22] used FEM to numerically analyze inclined MHD ferrofluid flow in a wavy cavity. It looked into parameters like AR = 0.02-0.08, γ = 0°-90°, ϕ = 0-0.06, and Ra = 10-5. The findings indicated that while Nu_{avg} decreased with wavy surface amplitude (AR), increasing Ha increased Bejan number. For validation, velocity and isotherm profiles were contrasted.

The study by Khan et al. [23] used THNF and set the ranges (Re = 100-1500, ϕ = 1-10%) to numerically analyze the cooling of a 3D annulus PV/T system. For conjugate heat transfer, COMSOL Multiphysics was used. The average Nusselt number decreased by 21-28% as the concentration of nanoparticles increased, improving electrical efficiency to 9.3834% (blade-shaped, Re = 1500, ϕ = 10%). 85.62% was the maximum thermal efficiency. Trihybrid nanofluid flow over a disk was numerically examined by Galal et al. [24], taking into account Marangoni convection, porous media, gyrotactic microbes, and thermal radiation. It investigated mass and heat transport using LTNE/LTE models. The findings demonstrated that a higher interphase heat transmission factor enhanced the rates of heat transfer in both the liquid and solid phases, supporting thermal control in devices such as electronic devices and microreactors. Using THNF in a 3D roof prism with a rotating cylinder, the study by Xia et al. [25] numerically examined a novel cooling application. Effects on heat distribution were evaluated using COMSOL simulations (Re = 100–500, shape factor = 3–8.9, ϕ = 1–10%, rotation = 0.1–0.4 m/s). To maximize cooling, it assessed the Darcy-Weisbach friction factor, Nusselt number, and average outlet temperature.

The study by Alammari et al. [26] used forced convection and THNF (water/cobalt/zinc/silver) with copper cylinders to numerically assess the performance of a PV/T system. Nusselt number improved ~420-466% at 20% volume fraction, and fluid force increased ~1200-1300% with Re, according to turbulent simulations (Re: 10k-100k, ϕ: 1-20%, AR: 0.1-0.3), increasing PV cell efficiency by 9%. Predictive models were created using machine learning. The study by Rehman et al. [27] used FEM to numerically analyze mixed convection of a non-Newtonian fluid in a square cavity with obstacle. Using power-law indices (0.5, 1.0, 1.5), parameters such as Re, Richardson number (Ri), and obstacle gap (0.2–0.6) were examined. The average Nusselt number rose with greater Ri and wider obstacle gaps. According to the results, suggesting enhanced heat transfer.

Majeed et al. [28] conducted a numerical analysis of heat transfer in a sinusoidal cavity filled with oxide nanofluids, taking into consideration of nanoparticle shape factor, volume fraction, Reynolds number and inclined magnetic field. They showed that at ϕ = 2%, the Nusselt number was 7% higher with 1.89× greater kinetic energy and inferences to heat transfer were reduced as Hartmann numbers increased. Similarly, Ullah et al. [29] investigated conjugate heat transfer and entropy generation in an enclosure with a conducting cylinder and nanofluid under the influence of a magnetic field. Their work showed the Nusselt number deviated 11% to that of the neutral isothermal body at dimensionless conductivity = 5, while maintaining its closeness to an adiabatic body. In more biomedical related research, Alqurashi et al. [30] investigated hybrid nanoliquid blood flow with silver-gold nanoparticles under the effects of an inclined magnetic field using the Yamada-Ota and Hamilton-Crosser models. The models indicated a relatively higher nanoparticle volume fraction decreased velocity of flow, while Yamada-Ota was more efficient in terms of heat transfer. Extending further to non-Newtonian flow, Majeed et al. [31] investigated the flow around two cylinders with visco-plastic fluid using FEM, the Newton and PARDISO solvers. They showed that drag and lift coefficients were strongly dependent on gap spacing ratio (GP), while velocity increased flow at a higher Reynolds number with a lower Bingham number. The drag and lift forces increased with a smaller gap spacing ratio with both drag and lift forces increased with smaller gap spacing.

Khan et al. [32] examined irreversible unsteady viscous flow over a vertical plate using a Laplace transform & concluded that reducing thermal radiation decreased total entropy generation, whereas increasing heat transfer significantly added to total entropy. Also, Khan et al. [33] explored dusty fluid flow between two parallel plates using PLPT & noted that wall shear stress and wall stress/velocity increased when the Grashof number increased, while increasing the magnetic and radiation parameters decreased both wall stress/velocity. Rehman et al. [34] analyzed the effect of Marangoni convection in blood-bio-nanofluids based on carbon nanotubes (CNTs) and found that a greater nanoparticle volume fraction increased the temperature of the fluid between one hot and one cold portion of an object. They also found that single-wall CNTs produce a greater enhancement in Nusselt number and skin friction than multi-wall CNTs. To take this one step further, Khan et al. [35] examined the entropy generation in unsteady MHD (Magnetohydrodynamic) flow through a porous medium taking into account heat and mass transfer. They argued wall shear stress was an effective way to minimize entropy generation and that increasing the Grashof (Gr) and Prandtl (Pr) numbers would increase the Bejan number (the ratio of irreversibility; entropy generation to thermal energy transfer). In particular, they contended that energy loss minimization could be maximized by choosing favorable parametric values. In summary, the different studies above show that entropy generation and heat transfer could potentially be controlled by governing parameters in a complex system.

The literature and experiments conducted by Elsherbiny et al. [36, 37] involved the use of hybrid nanofluids in microchannels and worked through enhancement concepts, coolant–sink interactions, and gap analysis. Overall, the analysis suggested improved Nusselt number (Nu) and heat transfer coefficient (HTC) with different loads and concentration ratios, but hybrid nanofluids did underperform with respect to base fluids in some cases.

Novelty and Research Gap: The present study introduces significant novelty by comprehensively analyzing MHD, THNF flow and heat transfer within a ventilated cavity containing two distinct hot obstacles. While existing literature (e.g., Priam et al. [1], Ali et al. [15], Khan et al. [23]) have individually explored aspects like mixed convection, nanofluids, magnetic fields, or various cavity geometries, the synergistic interaction of a THNF with an electromagnetic field in this specific, multi-obstacle ventilated configuration remains largely unexplored.

Specifically, a notable research gap exists as most prior work focused on natural convection in cavities, and there is a distinct lack of studies applying advanced ternary nanofluids in such systems. Furthermore, the influence of the direction or angle of the magnetic field attack has been largely unexplored. This research directly addresses these gaps by also investigating six critical parameters, including the magnetic field angle, and uniquely determining optimal conditions for both minimum average entropy generation and minimum average Nusselt number for insulation.

Our research distinguishes itself through the concurrent investigation of six critical parameters: Ha, magnetic field angle, Re, nanoparticle shape factor, obstacle gap, and total nanoparticle volume fraction, with forced convection conditions imposed. Furthermore, we uniquely determine optimal conditions for both minimum average entropy generation and, notably, minimum average Nusselt number for insulation purposes. This dual optimization within the complex MHD ternary nanofluid system past multiple hot obstacles represent a novel contribution to thermal management design.

Choice of Nanoparticles: The selection of iron oxide (Fe_2O_3), copper oxide (CuO), and Molybdenum disulfide (MoS_2) as a THNF is necessary due to their complementary characteristics as individual nanoparticles and individual thermophysical properties as separate fluids and their potential for augmented thermophysical effectiveness for the hybrid fluid itself [40, 41]. Each of these nanoparticles has inherent advantages that will, in performance, improve the fluid's thermal performance more than a symmetric, or binary, nanofluid can provide. CuO and Fe_2O_3 both possess high thermal conductivities that directly contribute to the improved heat transfer inside the nanofluid. MoS_2 is a transition metal di-chalcogenide that is layered, it also has high lubricating properties, which can provide detailed insight into fluid friction and improve stability; an oxide, a metal oxide, and layered nanomaterial, a unique nanoparticle network can be accomplished through the combination of these nanoparticles within the base fluid.

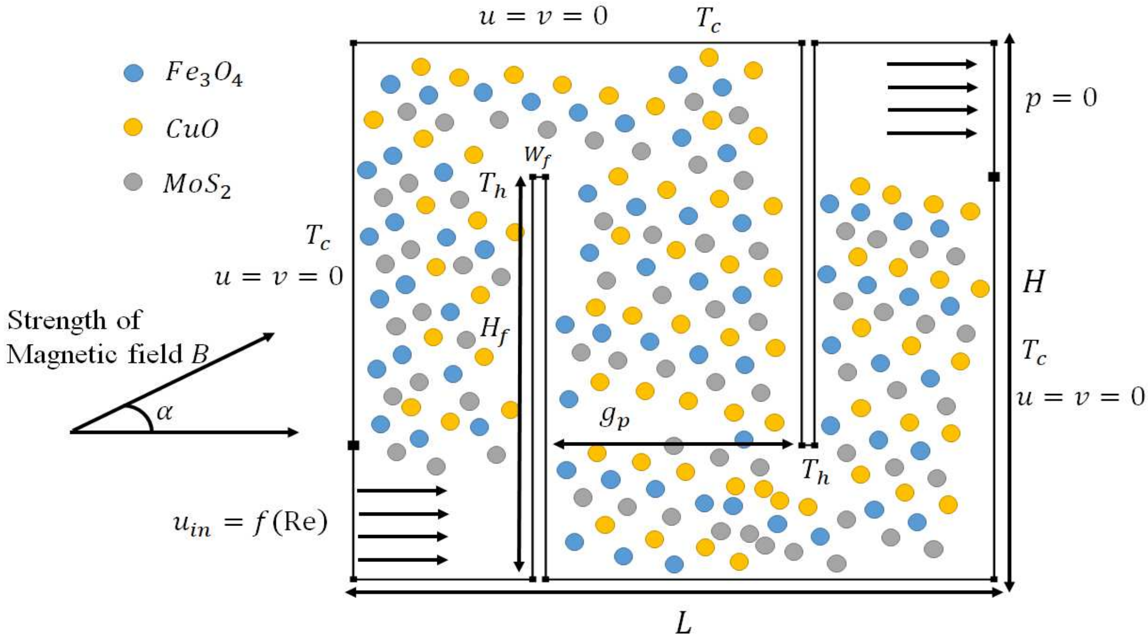

Fig. 1. Channel description for fluid flow and heat transfer modeling, detailing geometry and boundary conditions.

2. Methodology

2.1. Description of the channel and nanofluids

Figure 1 meticulously details the computational domain for our fluid flow and heat transfer analysis. It illustrates a rectangular cavity of length `$L$` and height `$H$`, containing two vertical rectangular obstacles of height `$H_f$` and width `$W_f$`, separated by a gap `$gp$`. These obstacles act as heat sources, maintained at a hot temperature `$T_h$` on their inner surfaces, while the external walls are kept cold at `$T_c$`. Fluid enters from the left inlet at a velocity `$u_{in}$`, determined by the Re, and exits from the right outlet at reference pressure `$p = 0$`. The fluid itself is a THNF, composed of Fe_3O_4, CuO, and MoS_2 nanoparticles, visually represented by distinct colored dots. Crucially, a magnetic field `$B$` is applied at an angle `$\alpha$` introducing Lorentz forces that influence the flow and heat transfer within the system.

Table 1 quantifies the geometric and boundary conditions shown in Fig. 1. It specifies `$L$` and `$H$` as 1 meter each, defining a square cavity. The obstacles are sized at `$0.75H$` height and `$0.02L$` width. The gap `$gp$` is a variable parameter, tested at 0.2, 0.4, and 0.6. The table provides formulas for the channel's open area (`$A_c$`) and hydraulic diameter (`$d_h$`), essential for flow calculations. The magnetic field angle `$\alpha$` is set $(0 - \pi/2)$. The Re ranges from 500 to 2000, and the inlet velocity `um` is derived from this. Finally, the hot and cold temperatures are fixed at `$T_h = 40^\circ C$` and `$T_c = 30^\circ C$`, respectively, establishing the thermal gradient.

Table 1. Comprehensive list of geometric parameters and associated boundary conditions shown in Fig. 1.

Symbols	Expression/value	Detail
L	1 (m)	Total length of the cavity
H	1 (m)	Total Height of the cavity
H_f	$0.75H$ (m)	Height of the obstacle
W_f	$0.02L$ (m)	Width of each obstacle
gp	0.2, 0.4, 0.6 (m)	Gap between the obstacle
A_c	$LH - 2(WH)_f$ (m^2)	Net area of the channel
P_r	$2(L + H + W_f) + 4H_f$ (m)	Total perimeter of the cavity
d_h	$4A_c / P_r$ (m)	Formula to compute the hydraulic diameter
α	$0 - \pi / 2$	Angle to launch the magnetic field
Re	500-2000	Reynolds number
u_{in}	$(\mathrm{Re}\,\mu_{thnf}) / (\rho_{thnf} d_h)$ (m/sec)	Velocity at the inlet section
T_c	$30^\circ C$	Temperature along cold walls
T_h	$40^\circ C$	Temperature along the obstacles

Table 2. Nanoparticle and Base Fluid Properties Influencing Thermal and Electromagnetic Field Interactions [28].

Nanoparticles and base fluid	c_p (J/kgK)	κ (W/mK)	ρ (kg/m^3)	σ (S/m)
H_2O	4179	0.613	997.1	2.09E-5
Fe_2O_3	670	9.7	5180	2.5E-4
CuO	531.8	76.5	6320	0.069
MoS_2	397.75	34.5	5060	0.05

Table 3. Detailed Parameters and Corresponding Equations for Calculating the Thermophysical Properties of THNF and see the detail in [25, 26].

Viscosity of THNF: $$\mu_{thnf} = \frac{\mu_{H_2O}}{(1-\phi_1)^{2.5}(1-\phi_2)^{2.5}(1-\phi_3)^{2.5}}$$

Thermal conductivity of HNF: $$\kappa_{hnf} = \kappa_{nf}\frac{\kappa_{CuO} + (n-1)\kappa_{nf} - (n-1)\phi_2(\kappa_{nf} - \kappa_{CuO})}{\kappa_{CuO} + (n-1)\kappa_{nf} + \phi_2(\kappa_{nf} - \kappa_{CuO})}$$

Thermal conductivity of THNF: $$\kappa_{thnf} = \kappa_{hnf}\frac{\kappa_{Fe_2O_3} + (n-1)\kappa_{hnf} - (n-1)\phi_1(\kappa_{hnf} - \kappa_{Fe_2O_3})}{\kappa_{Fe_2O_3} + (n-1)\kappa_{hnf} + \phi_1(\kappa_{hnf} - \kappa_{Fe_2O_3})}$$

Thermal conductivity of NF: $$\kappa_{nf} = \kappa_{H_2O}\frac{\kappa_{MoS_2} + (n-1)\kappa_{H_2O} - (n-1)\phi_3(\kappa_{H_2O} - \kappa_{MoS_2})}{\kappa_{MoS_2} + (n-1)\kappa_{H_2O} + \phi_3(\kappa_{H_2O} - \kappa_{MoS_2})}$$

Total volume fraction of THNF: $\phi = 0.01,\ 0.04,\ 0.07,\ 0.1$

Viscosity of water: $\mu_{H_2O} = 0.00089(Pas)$

Volume fraction of Fe_2O_3: $\phi_3 = (1/3)\phi$

Volume Fraction of CuO: $\phi_2 = (1/3)\phi$

Volume fraction of MoS_2: $\phi_1 = (1/3)\phi$

Heat Capacitance: $$(\rho c_p)_{thnf} = \Big((1-\phi_1)\Big((1-\phi_2)\Big((1-\phi_3)(\rho c_p)_{H_2O} + \phi_3(\rho c_p)_{MoS_2}\Big) + \phi_2(\rho c_p)_{CuO}\Big) + \phi_1(\rho c_p)_{Fe_2O_3}\Big)$$

Density of THNF: $$\rho_{thnf} = \Big((1-\phi_1)\Big((1-\phi_2)\Big((1-\phi_3)\rho_{H_2O} + \phi_3\rho_{MoS_2}\Big) + \phi_2\rho_{CuO}\Big) + \phi_1\rho_{Fe_2O_3}\Big)$$

Electrical conductivity of NF: $$\sigma_{nf} = \sigma_{H_2O}\frac{\sigma_{MoS_2}(1+2\phi_1) + 2\sigma_{H_2O}(1-\phi_1)}{\sigma_{MoS_2}(1-\phi_1) + \sigma_{H_2O}(2+\phi_1)}$$

Electrical Conductivity of HNF: $$\sigma_{hnf} = \sigma_{nf}\frac{\sigma_{CuO}(1+2\phi_2) + 2\sigma_{nf}(1-\phi_2)}{\sigma_{CuO}(1-\phi_2) + \sigma_{nf}(2+\phi_2)}$$

Electrical conductivity of THNF: $$\sigma_{thnf} = \sigma_{hnf}\frac{\sigma_{Fe_2O_3}(1+2\phi_3) + 2\sigma_{hnf}(1-\phi_3)}{\sigma_{Fe_2O_3}(1-\phi_3) + \sigma_{nf}(2+\phi_3)}$$

Table 2 provides the fundamental thermophysical and electromagnetic properties of the base fluid (H_2O) and the three distinct nanoparticles (Fe_2O_3, CuO, MoS_2) used in our water based THNF. Specifically, it lists their specific heat capacity (c_p), thermal conductivity (κ), density (ρ), and electrical conductivity (σ). These inherent material properties are the foundational inputs for calculating the overall properties of advanced THNF. For instance, the high thermal conductivity of Fe_2O_3, CuO and MoS_2 nanoparticles, compared to water, is key to the nanofluid's enhanced heat transfer capabilities, while their densities influence the nanofluid's overall density. The electrical conductivities of the nanoparticles and water are crucial for determining the nanofluid's electrical conductivity, which directly impacts the magnetic field's influence on the fluid flow through Lorentz forces.

Table 3 details the mathematical expressions and key parameters required to compute the effective thermophysical properties of the (THNF). These equations are essential for accurately modeling the fluid's behavior in the cavity channel handled the hot fins. The table includes models for the viscosity, thermal conductivity, heat capacitance, density, and electrical conductivity of the nanofluid, showing how these are derived from the individual properties listed in Table 2 and the volume fractions of each nanoparticle. The shape factor of a nanoparticle is a dimensionless value representing the physical geometry of the nanoparticles suspended in the nanofluid. In our model, we reduced this to a simplified shape factor. In practice, the shape factor is directly related to the fabrication of the particle and how the particle behaves in a suspension. Particle shape can substantially affect two critical thermophysical properties of a nanofluid: viscosity and thermal conductivity.

It also introduces the shape factor (n = 3.7 (cylindrical shape), 4.9 (Brick shape) and 5.7 (Platelets)), total volume fraction (ϕ), and individual volume fractions (ϕ_1, ϕ_2, ϕ_3), which are crucial parameters for tailoring the nanofluid's properties and each of them taken to be (1/3) of the total volume fraction of the THNF. Finally, it defines Ha (Ha = 1, 25, 50) and the formula for the magnetic field effect (B). By using these equations and parameters, in the modeling and simulation for the fluid flow and heat transfer in cavity with hot obstacles can dynamically account for how varying nanoparticle concentrations, types, and magnetic field strengths influence the fluid's thermal and flow characteristics, enabling a comprehensive analysis of heat transfer and fluid dynamics within the cavity.

The research is centered on assessing the impact of six important parameters on the thermal and fluid dynamics of the system. These parameters and their definitions are as follows:

Reynolds Number (Re): Shows the ratio of the inertial forces to the viscous forces. Usage of this in the domain is to handle the velocity of the fluid and the intensity of the convection, with higher values indicating a more vigorous flow with enhanced heat transfer.

Hartmann Number (Ha): This number demonstrates the extent of the magnetic field's effect upon the fluid. It is defined as the ratio of electromagnetic force versus viscous force. Higher Ha represents stronger magnetic braking effects which reduces the fluid velocity and circulation with the greater fluidity.

Magnetic Field Angle (α): This element describes the angle of the external magnetic field imposed upon the fluid flow. The angle germane to the flow will affect the magnitude and direction of the Lorentz force, which will then manipulate the flow characteristics and heat transfer.

Total Nanoparticle Volume Fraction (ϕ): This whole volume percent is the total amount of the 3 nanoparticles in the basal fluid. Increasing the volume fraction improves the thermal properties of the fluid and increases the heat transfer performance.

Nanoparticle Shape Factor (*n*): This is the physical shape of the nanoparticle, such as a cylindrical, or brick, or platelets, etc. The shape of the particles impacts the fluid's thermal properties, especially the thermal conductivity and viscosity of the fluid, impacting heat transfer.

Gap between the hot obstacles (*gp*): This constraining parameter is the physical distance of the two heated obstacles. The distance automatically constrains the patterns of fluid flow, causing the flow to either accelerate or simply become more diffused depending on the size of the gap. This ultimately affects local velocities and ultimately the heat transfer.

THNF are a new type material to raise the rate of the heat transfer fluids with three distinct types of nanoparticles suspended in the base fluids like the water and the oil. THNF are different from traditional mono nanofluids (one type of nanoparticle) and binary nanofluids (two types of nanoparticles) because they create a synergism, which often results in better thermophysical properties.

The main benefits of THNF are:

Higher Thermal Conductivity: With three nanoparticles with impressive thermal conductivities (listed in Table 2), the resulting thermal network is often more complicated and efficient than those of mono or binary nanofluids, allowing for higher rates of heat transfer from the fluid.

Better Stability: The multitude of nanoparticles acts to improve the stability of the fluid by providing a better suspended and reduced agglomeration compared to mono nanofluids.

Customizable Properties: Using three nanoparticles allows the investigation of the specific thermal properties of the fluid by specifically making a selection of nanoparticle, with a defined volume fraction, to specifically fit a given application i.e., higher heat transfer coefficient for cooling versus lower heat transfer coefficient for insulation, is the major goal of this study.

2.2. Detail of governing equations and entropy generation

Equations (1) through (4) are the mathematical foundation to generate the numerical model, meticulously solved within COMSOL Multiphysics 6.2 to simulate fluid flow and heat transfer in two-dimensional cavity with a hot obstacle and magnetic field effect [38]:

$$\frac{\partial u}{\partial x}+\frac{\partial v}{\partial y}=0 \tag{1}$$

$$u\frac{\partial u}{\partial x}+v\frac{\partial u}{\partial y}=-\frac{1}{\rho_{thnf}}\frac{\partial p}{\partial x}+\frac{\mu_{thnf}}{\rho_{thnf}}\left(\frac{\partial^2 u}{\partial x^2}+\frac{\partial^2 u}{\partial y^2}\right)+\frac{\sigma_{thnf}B^2}{\rho_{thnf}}\left(v\sin(\alpha)\cos(\alpha)-u\sin^2(\alpha)\right) \tag{2}$$

$$u\frac{\partial v}{\partial x}+v\frac{\partial v}{\partial y}=-\frac{1}{\rho_{thnf}}\frac{\partial p}{\partial y}+\frac{\mu_{thnf}}{\rho_{thnf}}\left(\frac{\partial^2 v}{\partial x^2}+\frac{\partial^2 v}{\partial y^2}\right)+\frac{\sigma_{thnf}B^2}{\rho_{thnf}}\left(u\sin(\alpha)\cos(\alpha)-v\cos^2(\alpha)\right) \tag{3}$$

$$u\frac{\partial T}{\partial x}+v\frac{\partial T}{\partial y}=\frac{\kappa_{thnf}}{(\rho c_p)_{thnf}}\left(\frac{\partial^2 T}{\partial x^2}+\frac{\partial^2 T}{\partial y^2}\right) \tag{4}$$

Equation (1), the continuity equation, ensures mass conservation for the incompressible fluid. It guarantees that the fluid flow field is physically realistic, dictating how the velocity components (u in x-direction, v in y-direction) must relate to maintain constant density. Equations (2) and (3) are the x and y momentum equations, respectively, derived from the Navier-Stokes equations. These describe how forces govern the fluid's motion. Each equation includes terms for inertial forces (momentum transport by fluid motion), pressure gradients (driving force from pressure differences), and viscous diffusion (internal friction due to fluid viscosity). Crucially, these equations incorporate a Lorentz force term, proportional to the nanofluid's electrical conductivity (σ_{thnf}) and the magnetic field strength (B) and its angle (α). This term quantifies the magnetic field's direct influence on the fluid's velocity components, introducing (MHD) effects that can either impede or enhance flow.

Equation (4) is the energy equation, representing the conservation of heat. It describes how temperature (T) changes within the fluid due to convective heat transfer (heat carried by the bulk fluid motion) and conductive heat transfer (heat diffused through molecular interactions). The nanofluid's thermal conductivity (κ_{thnf}) and volumetric heat capacity ($(\rho c_p)_{thnf}$) are key parameters here, governing the efficiency of heat distribution.

Entropy generation via thermal distribution:

$$S_{HT}=\frac{\kappa_{thnf}}{T_m^2}\left(\left(\frac{\partial T}{\partial x}\right)^2+\left(\frac{\partial T}{\partial y}\right)^2\right) \tag{5}$$

Entropy generation via the friction of fluid:

$$S_{FF}=\frac{\mu_{thnf}}{T_m^2}\left(2\left(\frac{\partial u}{\partial x}\right)^2+2\left(\frac{\partial v}{\partial y}\right)^2+\left(\frac{\partial u}{\partial y}+\frac{\partial v}{\partial x}\right)^2\right) \tag{6}$$

Entropy generation due to MHD:

$$S_{MHD}=\frac{\sigma_{thnf}B^2}{T_m}\left(u\sin(\gamma)-v\cos^2(\gamma)\right) \tag{7}$$

Here T_m is the mean temperature.

Total entropy generation:

$$S_{tot}=S_{HT}+S_{FF}+S_{MHD} \tag{8}$$

The entropy generation framework was derived from the thermodynamic principles established by Bejan [43] and later elaborated by Mahmud and Fraser [44] to account for irreversibility arising from heat transfer, fluid friction, and magnetic effects in magnetohydrodynamic (MHD) flows. The governing equations (1) to (4) incorporated these effects, and entropy generation was minimized as summarized in Table 3.

Equations (5) to (8) quantified the entropy generation, a fundamental concept for evaluating thermodynamic irreversibility and energy efficiency [27]. Equation (5) expressed the entropy generation due to heat transfer (S_{HT}), indicating losses associated with temperature gradients. Equation (6) represented the entropy generated by fluid friction (S_{FF}), corresponding to viscous energy dissipation. Equation (7) introduced the magnetic contribution (S_{MHD}), resulting from Ohmic heating due to the interaction between the magnetic field and the conducting fluid. The total entropy generation (S_{tot}) in Eq. (8) was obtained as the sum of these components, offering a comprehensive measure of overall energy degradation.

By minimizing (S_{tot}), the model and simulations aimed to optimize the system's energy efficiency by identifying the dominant sources of irreversibility thermal, frictional, or magnetic—under varying operating conditions. These three mechanisms of energy dissipation are physically distinct yet occur simultaneously, which justifies representing the total entropy generation as the additive sum of the individual contributions, consistent with the principles of irreversible thermodynamics under local thermodynamic equilibrium.

Other Computational parameters [25, 26]:

Local Nusselt number:

$$Nu_x = \left(\frac{h_{cf}}{\kappa_{thnf}}\right)x_{wall} \tag{9}$$

Average Nusselt Number:

$$Nu_{avg} = \frac{1}{L_w}\int_0^{L_w} Nu_x dx \tag{10}$$

Heat Transfer Coefficient:

$$h_{cf} = \frac{k_{thnf}}{T - T_{bulk}}\frac{\partial T}{\partial x} \tag{11}$$

Bulk Temperature:

$$T_{bulk} = \frac{\int_0^H uTdx}{\int_0^H udx} \tag{12}$$

Prandtl Number:

$$\Pr = \frac{\mu_{thnf}(c_p)_{thnf}}{\kappa_{thnf}} \tag{13}$$

These computational parameters are invaluable post-processing tools, translating raw simulation data into meaningful performance metrics for our fluid flow and heat transfer analysis. The Local Nusselt number (Nu_x), defined in Eq. (9), quantifies the convective heat transfer efficiency along the wall, showing where heat exchange is most effective. Building on this, the Average Nusselt Number (Nu_{avg}) from Eq. (10) provides a single, overall measure of heat transfer performance for an entire wall along the domain, crucial for comparing different design configurations or operating conditions.

To calculate the Nusselt numbers, the Heat Transfer coefficient (h_{cf}) (Eq. (11)) is determined, which measures the rate of heat exchange between the solid surfaces and the flowing nanofluid. This requires the Bulk Temperature (T_{bulk}), calculated via Eq. (12), representing the average temperature of the fluid across the domain of the interest, providing a more representative value for heat transfer calculations. Lastly, the Prandtl Number (Pr), described in Eq. (13), is a dimensionless property comparing the nanofluid's momentum and thermal diffusivities. It helps interpret the relative thicknesses of velocity and thermal boundary layers, explaining how efficiently heat is transported relative to momentum in the flow.

The following assumptions have been made for the present study

- The study is assumed to be two-dimensional and time-dependent due to the closed nature of the channel.
- The thermal and physical properties of the nanoparticles and the base fluids are assumed to be independent of time and temperature because of the small difference between the low and high temperatures.
- The base fluid, water, is assumed to be incompressible and non-Newtonian. This means the viscosity of the water is constant, and the effects of shear thickening and shear thinning are ignored.
- There is no suppressed backflow at the channel's outlet, and the pressure there is assumed to be zero.
- The source or forcing function in the Navier-Stokes equation is assumed to be zero, and the buoyancy effect is also assumed to be zero.

2.3. Finite element procedure for governing equations

It is evident that the finite element procedure for the governing equations of fluid flow and heat transfer follows a systematic, multi-phase procedure. The method allows for the transformation of the complex partial differential equations (PDEs) into a single set of algebraic equations to facilitate numerical solutions. For the first stage, the discretization of the domain will take place, which is means that we will be taking the physical space of the ventilated cavity with its two obstacles and dividing that space into finite numbers of elements that are interconnected as a mesh. Figure 2 presents refined mesh, which is typically done for accuracy in a solution even more so in regions with high gradients. The work done in defining the finite element mesh has transformed the continuous problem into a discrete collection of nodes and elements to enable numerical approximations.

Next comes the derivation of element equations. For each individual element, the governing PDEs (continuity, momentum and energy (1)-(4)) are reformulated as a simplified algebraic representation, using the Galerkin method or a weak formulation. In this process the PDE is multiplied by a weighting function (w) and integrated over the volume of the element. In addition, the unknowns (e.g., velocity, pressure, temperature, etc.) are captured using shape functions that interpolate the solution between the nodes of the element. This results in a matrix system for each individual element that relates the nodal values of the unknowns.

Next, the "element equations" are assembled to become global equations. The element equations can then be assembled to become a large, single set of algebraic equations representing the entire domain by simply summing all contributions from each element at each of their respective shared nodes. The end result is a global stiffness matrix, a global force vector, and a global vector of all unknown nodal values, or ([*K*][*X*] = [*F*]).

Applying the boundary conditions is an important step. After applying the boundary conditions, it is where the boundary conditions, or specific constraints associated with our problem is applied. The description shows several conditions: no-slip conditions present on the walls of the cavity and obstacle (zero velocity), inlet velocity and temperature of the fluid, and a zero-pressure outlet (which is effectively atmospheric pressure). Thermal boundaries are defined, with hot obstacles and cold cavity walls. The boundary conditions are going to adjust the global matrix and global vector. The important point here is that the boundary conditions will make sure that the final solution is physically possible.

Once all of the physics has been assembled and boundary conditions applied, the system of equations can be solved, to find the value of the unknown scalars at each node. Because the governing equations are also non-linear, and iterative solver will be used to solve the system of equations. Solving the momentum and energy equations will often be done in a coupled manner, where the solution is being refined at each iterative step, until a predetermined criterion for convergence is met.

2.4. COMSOL working procedure

To find the numerical solution for fluid flow and heat transfer problems, the finite element-based software COMSOL Multiphysics is an essential and successful tool [23, 25, 26]. It effectively tackles the governing equations related to these phenomena for numerical analysis. COMSOL Multiphysics' user-friendly environment provides us with greater flexibility to solve Multiphysics problems that combine fluid flow, heat transfer, and electromagnetic forces in the presence of THNF. The following steps outline the feasibility of programming within the software.

Step 1: Define all the parameters in the *Definitions* section as listed in Fig. 1 and Tables 1 to 3.

Step 2: Define the variables that will be used for post-processing. In this case, the local Nusselt number, average Nusselt number, and bulk temperature are the primary variables included in the post-processing analysis.

Step 3: Draw the geometry of the cavity using the dimensional parameters specified in Table 1. This should include the obstacle, and the gap between obstacles must be properly justified.

Step 4: Assign the appropriate materials to the geometry based on the information provided in Tables 2 and 3.

Step 5: Apply the boundary conditions for each physics interface. In this case, both fluid flow and heat transfer physics are used.

Step 6: Perform a mesh independence study to minimize numerical error in the computations, and conduct a validation by comparing the results with available literature.

Step 7: Conduct a parametric study using variables such as shape factor and Re as the primary parameters.

Step 8: Carry out the post-processing steps to analyze and interpret the simulation results.

3. Mesh Refinement and Literature Comparison

Figure 2 presents the mesh independence test for the non-dimensional velocity (u/u_{in}) and the non-dimensional temperature (θ temperature profile) using irregular triangular meshes within COMSOL Multiphysics. This test is crucial to ensure that the numerical results are independent of the mesh density, thereby guaranteeing accuracy and reliability. The analysis is conducted under fixed parameters: (Re = 2000), gap size (gp = 0.2), (Ha = 50), volume fraction (ϕ = 10%), shape factor (n = 5.7), and magnetic field angle (α = 90°).

For the non-dimensional velocity (u/u_{in}), as the number of elements increases, the value initially fluctuates but then progressively stabilizes and approaches a constant value. Beyond approximately 22,000 elements, the change in non-dimensional velocity becomes negligible, indicating that the solution has become independent of further mesh refinement. This stabilization signifies that the chosen mesh density is sufficient to accurately capture the fluid velocity field.

Similarly, for the non-dimensional temperature (θ), as the number of elements increases, the value also exhibits an initial adjustment phase before settling. Beyond around 20,000 elements, the non-dimensional temperature curve flattens out, showing minimal variation with further increases in mesh elements. This confirms that the thermal solution is also independent of the mesh resolution.

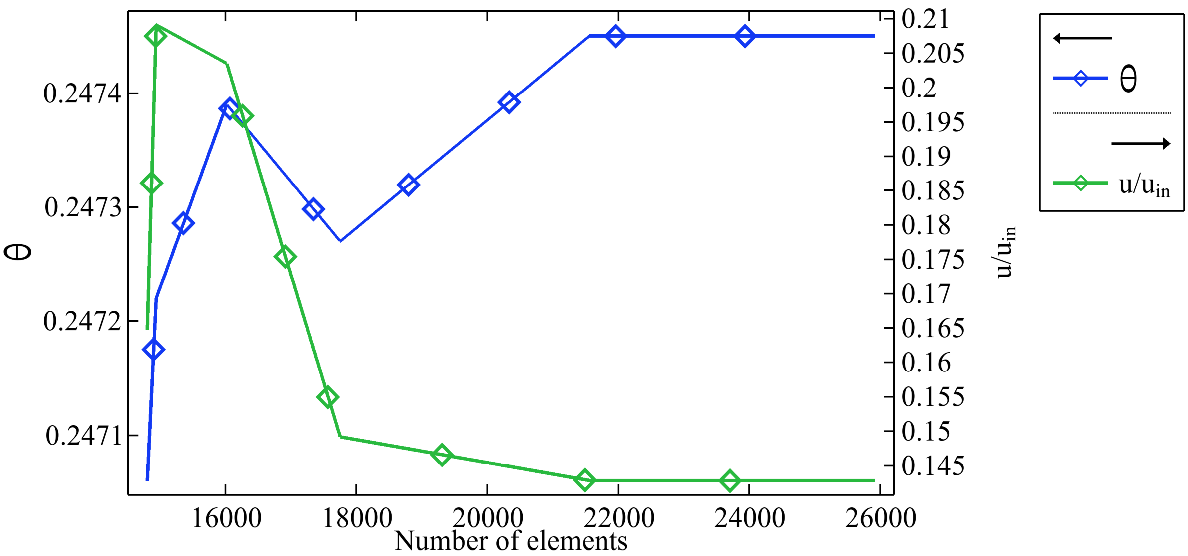

Fig. 2. The mesh independent test for the non-dimensional velocity (u/u_{in}) and the non-dimensional temperature $\theta = (T - T_c)/(T_h - T_c)$ keeping Re = 2000, gp = 0.2, Ha = 50, ϕ = 10%, n = 5.7, α = 90.

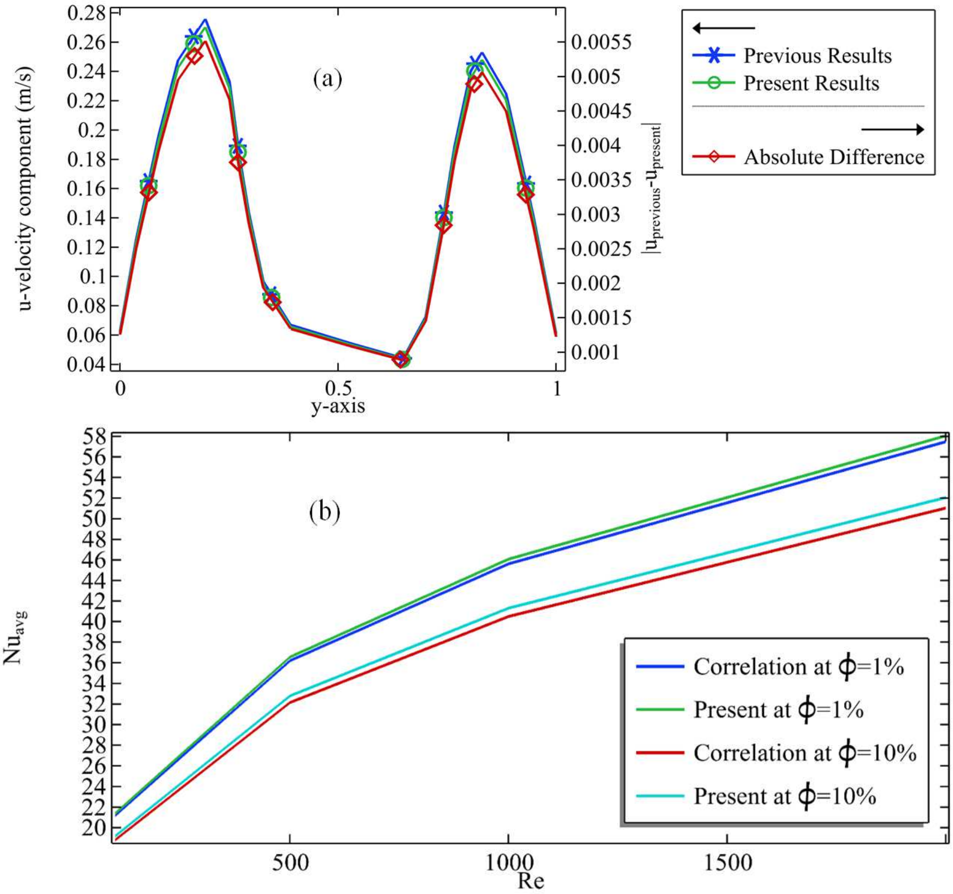

Fig. 3. (a) Validation of the computational work: Comparison of the u-velocity component along the vertical midline of the channel (y-axis) with established literature data [27], highlighting the deviation between previous and current computational values, (b) Comparison of the average Nusselt number at the middle of the channel with the Re using THNF volume fractions of 1% and 10% with the correlation [39].

The overall trend for both parameters demonstrates that sufficient mesh refinement has been achieved, confirming the reliability of the computational model. The point at which both curves stabilize, typically around 20,000 to 22,000 elements, represents the optimal mesh size for balancing computational cost with accuracy for this specific numerical modeling and simulation. Based on the findings and discussed the mesh independence test, this work on the two-dimensional cavity with two obstacles was resolved with irregular triangular elements. This is due in part to the complexity in the geometry and conical tips of the hot vertical obstacles and a finer mesh is better to resolve gradients. The number of elements still limited to no more than 26,000 to ensure sufficient robustness for solutions.

The numerical calculations were carried out using the Parallel Array and Residual-based Distribution Iterative Solution Orchestration (PARDISO) solver. PARDISO is an efficient parallel direct solver that can solve a large-scale system of sparse linear equations reasonably well. This solver was useful for this research because we were solving complex finite element method (FEM) simulations that create large systems of sparse linear equations that can be inefficiently solved using traditional approaches. PARDISO allows for faster computation times and reduced memory usage.

The solution was deemed to be converged when less than 10^{-6} relative error was determined between two successive approximations for all simulations. This representative convergence criterion ensures that the numerical results we present here are accurate and reliable.

Figure 3(a) is a critical validation plot, comparing the u-velocity component along the vertical midline of the channel (y-axis) between the present computational work and existing literature results. The significance of this comparison lies in confirming the accuracy and reliability of the numerical model developed, particularly its ability to reproduce established benchmarks.

The graph clearly shows three distinct curves: "Previous Results" representing data from the literature, "Present Results" from the current simulation, and the "Absolute Difference" between them. It is explicitly stated that the previous work utilized the same geometry and a non-Newtonian fluid but ignored the electromagnetic field effect. For the purpose of this direct validation, the present simulation was run under identical conditions to the previous literature, meaning that for this specific plot, the electromagnetic field effect was also effectively "ignored" or set to match the previous work's conditions, ensuring a point-to-point comparison despite the broader study incorporating magnetic fields. The minimal difference strongly confirms that the current numerical model and its implementation are highly accurate in reproducing the fundamental fluid dynamics under the specific conditions of the validation case. This successful validation provides strong confidence in the reliability of the computational approach, even when subsequently applied to more complex scenarios involving magnetic fields and advanced nanofluids, will be explored.

Further validation is presented in Fig. 3(b), where the average Nusselt number versus Re is compared via the above correlation [39] for the present findings calculated at the channel center with two volume fractions (1% and 10%) of advanced ternary nanofluids. The findings indicate that the average Nusselt number has a positive, and approximate linear relation with Re since increasing Re yield higher velocity at the channel center which may positively correspond with heat transfer. Additionally, the average Nusselt numbers obtained in this study appear reasonable and correspond well with the average Nusselt numbers calculated using the correlation of Shah et al. [39], which further establishes that the numerical code developed and presented in this study is yielding reasonable results.

Table 4. Comparison of the Local Nusselt Number with a Previous Study on Natural Convection in a Square Cavity (Pr = 0.71, Ra = 10^6).

y-axis	Nu_{hot} (Previous study)	Nu_{hot} (Present study)	Percentage change (%)
0.00481	16.1616	17.1391	6.0483
0.02846	17.3716	18.1480	4.4694
0.04327	17.5227	18.1491	3.5748
0.06490	17.0997	18.1460	6.1190
0.10817	16.0121	17.1380	7.0317
0.14904	14.8036	15.1289	2.1978
0.20433	13.5952	14.1197	3.8578
0.25481	12.6284	13.1121	3.8304
0.31731	11.3293	12.1018	6.8183
0.47476	8.7915	9.0808	3.2903
0.54207	7.7644	8.0720	3.9630
0.61298	6.7674	7.0634	4.3741
0.66223	6.1329	7.0578	15.0802
0.69471	5.6798	6.0537	6.5845
0.86539	2.9607	3.0288	2.2976

The comparison in Table 4 assesses the local Nusselt number (Nu_{hot}) along the y-axis of a square cavity under natural convection, contrasting results from the present study with a previous study [42], both using a Prandtl number (Pr) of 0.71 and a Rayleigh number (Ra) of 10^6. The table lists Nu_{hot} values from the previous study (ranging from 2.9607 to 17.3716) and the present study (from 3.0288 to 18.1480), alongside percentage changes (2.1976% to 15.0802%), indicating the present study generally predicts higher heat transfer rates. This suggests potential differences in numerical approaches or modelling details, despite both employing the Finite Element Method in COMSOL Multiphysics, though deviations remain small and align with the previous study's high-fidelity benchmark (less than 0.2% deviation). The previous study, focusing on buoyancy-driven flow in a differentially heated square cavity, explores a wide range of Ra and Pr, showing a Nusselt number increase from 1.0 to 9.2 as Ra rises, driven by thermal boundary layers and vortices, with higher Pr enhancing localized heat transfer. Your current research on ventilated cavities with ternary hybrid nanofluids under an electromagnetic field builds on this by introducing complex factors like nanofluids and magnetic fields, using the comparison as a validation step, though slight Nu_{hot} increases may reflect enhanced conductivity or setup differences, warranting further exploration.

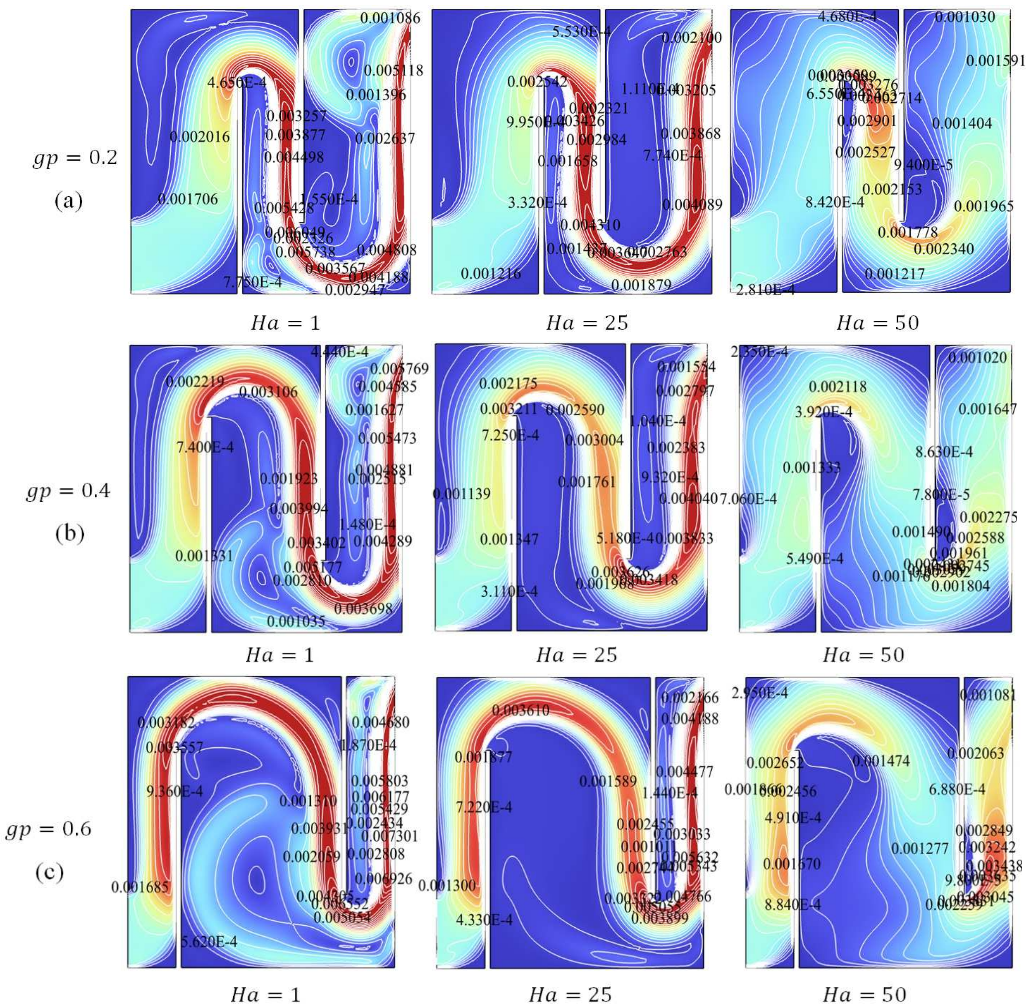

Fig. 4. (a) to (c) The presentation of the velocity distribution with the surface plots and the contours while fixing Re = 1000, ϕ = 10%, n = 5.7, α = 90°.

4. Results and Discussion

4.1. Velocity distribution with the surface plots and contours

Figures 4(a-c) comprehensively illustrate the velocity distribution within the computational cavity through detailed surface plots and overlaid contours. These visualizations critically reveal the combined influence of the (Ha) and the gap size (*gp*) between the internal obstacles on the fluid flow characteristics. The fixed parameters, including a Re of Re = 1000, a total volume fraction of ϕ = 1% for the THNF, a shape factor value of *n* = 5.7, and a magnetic field angle of α = 0°, ensure that the observed variations in flow patterns are directly attributable to Ha and *gp*.

A prominent and consistent observation across all panels is the inverse relationship between Ha and the fluid velocity. As Ha escalates from 1 to 50, the maximum velocity magnitudes visibly diminish, indicated by the shrinking of the vibrant red and orange regions and the expansion of the cooler blue zones. Correspondingly, the velocity contours become progressively less dense and more diffused, signifying a reduction in the steepness of velocity gradients throughout the flow domain. This phenomenon is a direct consequence of the Lorentz force, an electromagnetic body force that arises when the electrically conducting THNF traverses the applied magnetic field. With increasing (Ha), either the magnetic field strength or the nanofluid's electrical conductivity is augmented, leading to a more potent Lorentz force. This force fundamentally acts as a resistive or damping mechanism, effectively converting a portion of the fluid's kinetic energy into heat through Joule dissipation. This magnetic braking effect inherently increases the flow resistance, thereby suppressing the fluid's momentum and subsequently reducing its velocity. This explains the observed overall deceleration and the tendency for high-velocity core flows to be particularly attenuated at higher (Ha).

Beyond the magnetic influence, the physical geometry of the cavity, specifically the gap size (*gp*) between the obstacles, profoundly shapes the velocity distribution. Comparing the results for *gp* = 0.2 (Fig. 4(a)) with those for *gp* = 0.4 (Fig. 4(b) and 4(c)), distinct flow characteristics emerge. When the gap is narrower (*gp* = 0.2), the fluid flow experiences a significant constriction. According to the principle of mass conservation, the fluid must accelerate through this reduced cross-sectional area, leading to higher localized peak velocities within the constricted passages. This is manifested by tightly packed velocity contours in these regions. Moreover, the abrupt change in flow path caused by the smaller gap tends to induce more intense and well-defined recirculation zones both upstream and downstream of the obstacles. Conversely, a larger gap (*gp* = 0.4, 0.6) provides a less restrictive flow path. This results in generally lower peak velocities as the fluid is not compelled to accelerate as drastically. The velocity contours appear more spread out, indicating gentler velocity gradients across the wider channels. The recirculation patterns observed in larger gaps are typically less vigorous and more distributed, reflecting the reduced flow confinement. The collective interplay between the magnetic field's damping effect and the geometric constraints imposed by the obstacles provides a comprehensive understanding of how these parameters can be manipulated to achieve desired flow characteristics and optimize the performance of such complex fluidic systems.

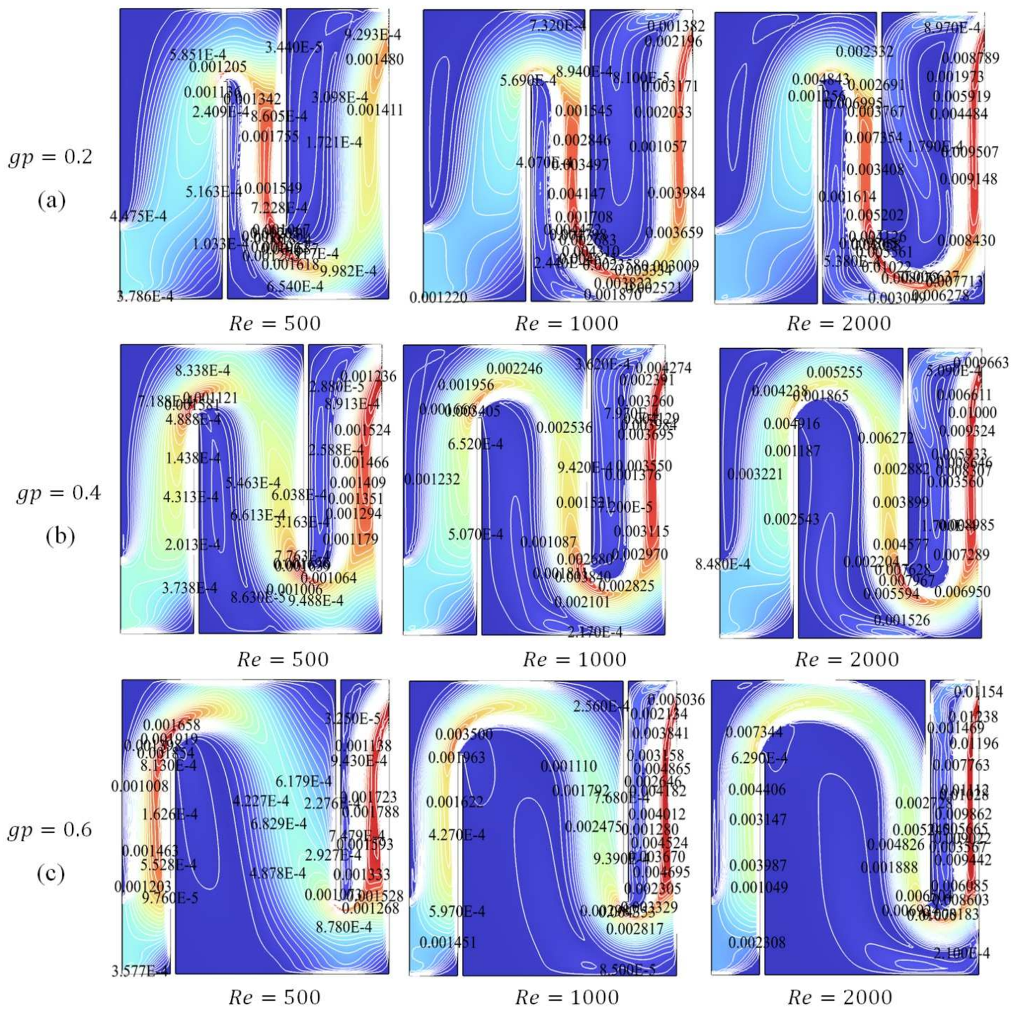

Fig. 5. (a) to (c) The presentation of the velocity distribution with the surface plots and the contours while fixing Ha = 50, ϕ = 10%, *n* = 5.7, α = 90°.

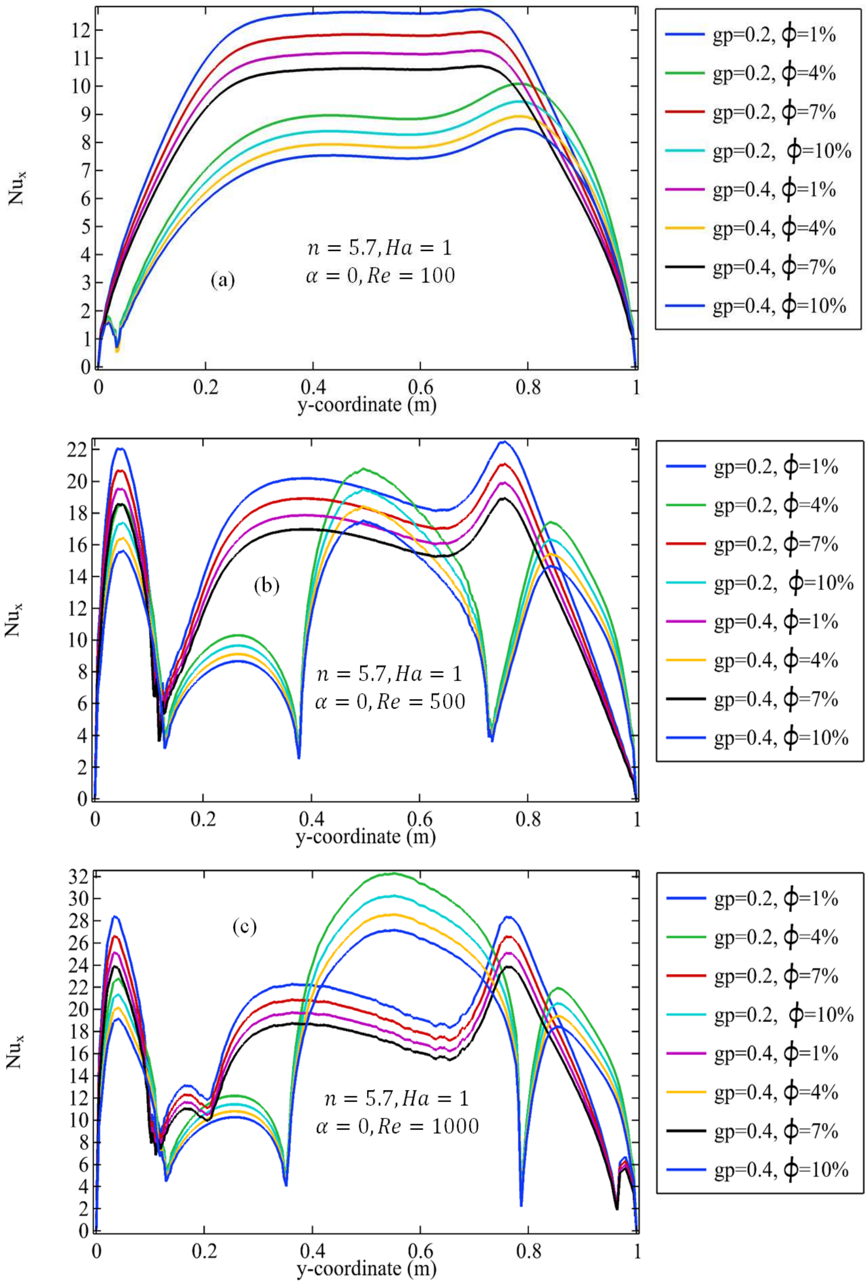

Fig. 6. (a) to (c) Sensitivity analysis of local Nusselt number distribution with variations in gap between obstacles, volume fraction of THNF, and Re.

Figures 5 (a-c) illustrates the velocity distribution within the cavity through surface plots and contours, highlighting the influence of both the gap (*gp*) between the obstacles and the Re. The plots maintain fixed parameters for (Ha = 50), volume fraction (ϕ = 10%), shape factor (*n* = 5.7), and magnetic field angle (α = 90°).

As the Re increases from Re = 500 to 2000, the fluid velocity generally increases, indicated by larger regions of red and orange, representing higher velocity magnitudes. This is a direct consequence of increased inertial forces overcoming viscous forces, leading to stronger fluid circulation and more intense flow patterns.

The gap size between the obstacles significantly impacts the velocity distribution. For a smaller gap, such as *gp* = 0.2 (Fig. 5(a)), the flow is more constricted, forcing the fluid to accelerate through the narrow passages. This leads to higher local velocities in these regions due to the principle of mass conservation. The contours are more tightly packed in these narrow areas. As the gap increases to *gp* = 0.4 (Fig. 5(b)) and *gp* = 0.6 (Fig. 5(c)), the flow path widens, reducing the constriction. This results in generally lower peak velocities compared to the smaller gap, as the fluid does not need to accelerate as much. The velocity contours appear less compressed, indicating gentler velocity gradients across the channel. This interplay between geometry and inertia dictates the complex velocity fields observed.

4.2. Sensitivity analysis for the local Nusselt number

The presented Fig. 6(a-c), meticulously illustrates the sensitivity of the local Nusselt number (Nu_x) distribution along a vertical line precisely at the channel's longitudinal midpoint (*x* = 0.5 (m)). This comprehensive analysis systematically investigates the impact of three critical parameters: the volume fraction (ϕ) of the THNF, the gap size (*gp*) between the internal obstacles, and (Re). Throughout this examination, specific parameters remain constant to isolate the effects: the shape factor is fixed at n = 5.7, Ha = 1, and the magnetic field angle at α = 0°.

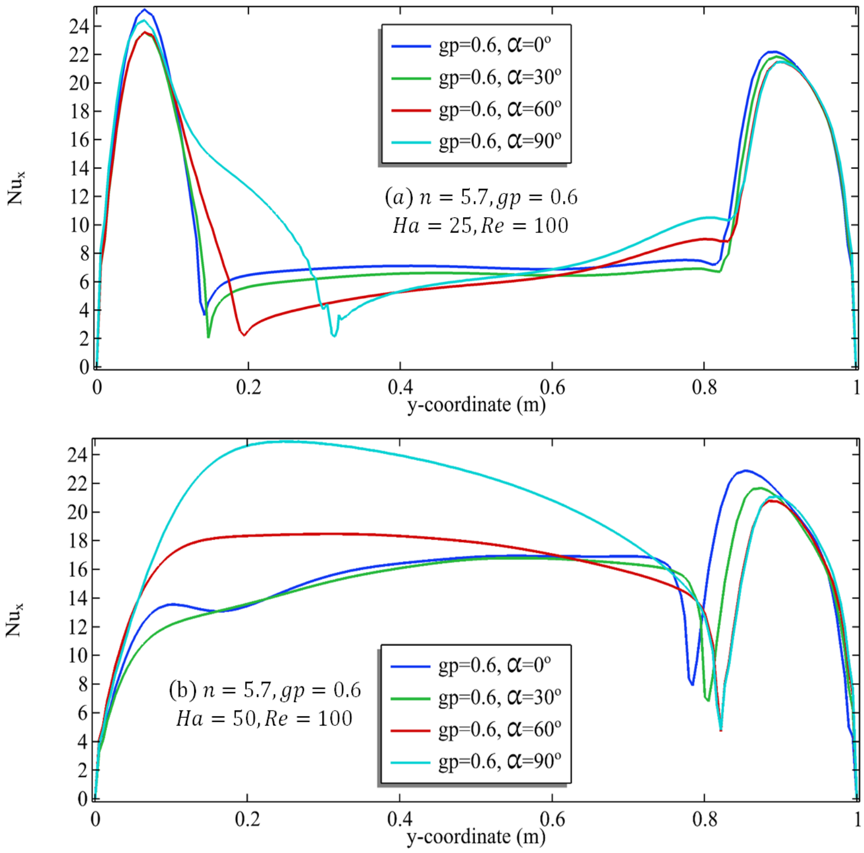

Fig. 7. (a) and (b) Sensitivity analysis of the local Nusselt number distribution with variations of angle of the magnetic field effect and the Ha.

A fundamental and consistent characteristic across all plotted curves, regardless of the varied parameters, is the oscillatory behavior of Nu_x along the y-coordinate. This is typically manifested with many prominent peaks see Figs. 6(b) and 6(c), corresponding to the locations where the fluid directly interacts with the heated surfaces of the internal obstacles. The local Nusselt number, being a measure of the convective to conductive heat transfer ratio, is directly proportional to the temperature gradient at the wall. Consequently, these peaks signify regions of maximal heat exchange where the temperature difference between the wall and the adjacent fluid is most pronounced. Conversely, the sharp drops or troughs in the curves typically occur in colder regions or areas where flow separation and reduced convection lead to less efficient heat transfer. This inherent pattern validates the expected thermal behavior within a channel containing hot obstructions.

The influence of the nanofluid's volume fraction (ϕ) on heat transfer is clearly demonstrated. For every combination of gap size and Re, an increase in the volume fraction consistently leads to a higher local Nusselt number see Fig. 6(c). This observation is directly rooted in the enhanced thermophysical properties of the nanofluid. As the concentration of nanoparticles within the base fluid increases, the effective thermal conductivity (κ_{thnf}) of the THNF is significantly improved, as per the established models for hybrid nanofluids. This augmented thermal conductivity facilitates a more rapid and efficient transfer of heat from the hot surfaces of the obstacles into the circulating fluid. The improved heat conduction within the fluid, coupled with the convective transport, results in steeper temperature gradients at the solid-fluid interface, thereby boosting the local Nusselt number and signifying superior heat transfer performance.

The geometric configuration, specifically the gap size (*gp*) between the obstacles, also exerts a substantial influence on the local heat transfer efficiency Fig. 6(a). A comparative analysis of the curves for $gp = 0.2$ (represented by blue, green, red, and cyan lines) against those for $gp = 0.4$ (magenta, orange, black, and navy lines) reveals that the smaller gap ($gp = 0.2$) generally promotes higher local Nusselt numbers across a broad range of volume fractions and Re. This can be physically explained by the flow dynamics induced by the reduced cross-sectional area. The narrower passages compel the fluid to accelerate, leading to increased local velocities and higher shear rates. This intensification of fluid motion and mixing within the constricted areas results in a thinner thermal boundary layer adjacent to the heated walls. A thinner thermal boundary layer inherently allows for a more efficient transfer of heat from the solid surface to the bulk fluid, thus enhancing convective heat transfer and manifesting as a higher local Nusselt number.

Finally, the impact of the Re on heat transfer is profoundly significant. By observing the progression from Fig. 6(a) (Re = 100) to 6(b) (Re = 500) and ultimately to Fig. 6(c) (Re = 1000), a very distinct trend emerges: increasing the Re leads to a substantial increase in the local Nusselt number. A higher Re indicates a more vigorous and dominant forced convection regime, characterized by higher fluid velocities and stronger inertial forces. This accelerated flow actively reduces the thickness of the thermal boundary layer along the heated surfaces, as the heat is more rapidly carried away by the moving fluid. Consequently, the temperature gradients at the wall become steeper, directly translating to an elevated rate of heat transfer from the obstacles into the nanofluid. The enhanced turbulent mixing (or intensified convective mixing even in laminar flows at higher Re) contributes to a more effective distribution of heat throughout the fluid, ultimately resulting in a significant improvement in overall heat dissipation capabilities as the Re increases.

Figures 7(a, b), provide critical insights into the local Nusselt number (Nu_x) distribution along the vertical midline ($x = 0.5$ m) of the channel. These graphs meticulously detail how the local heat transfer coefficient is influenced by variations in the magnetic field angle (α) and (Ha). Throughout this analysis, consistent parameters such as the shape factor ($n = 5.7$), gap between obstacles ($gp = 0.6$), and (Re = 100) are maintained.

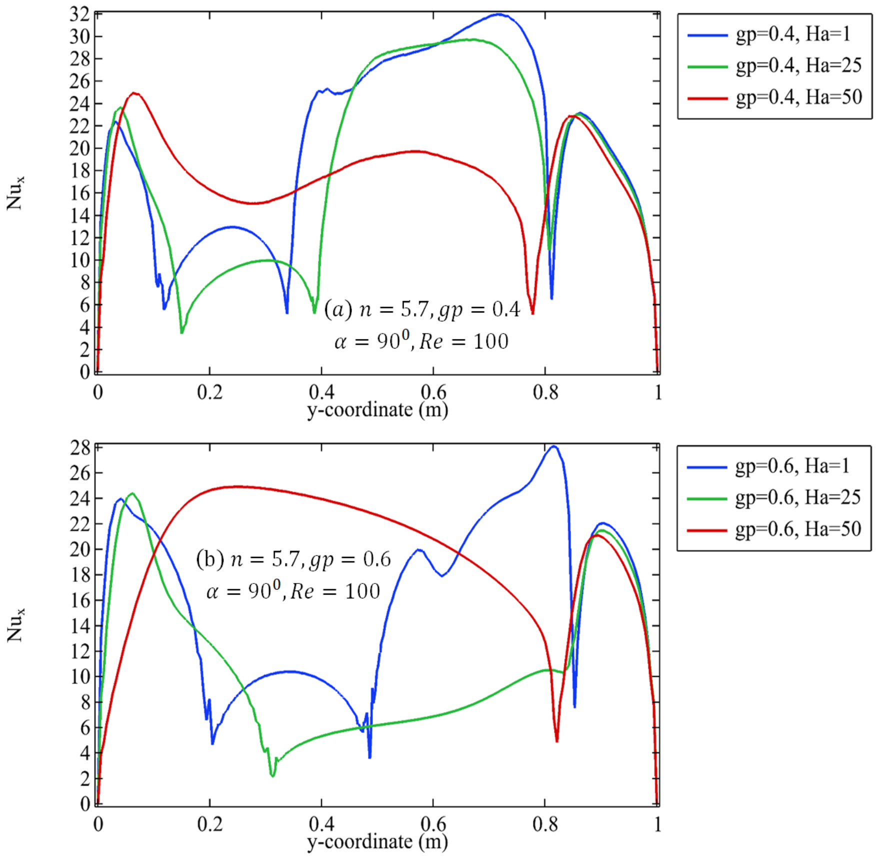

Fig. 8. (a) and (b) Sensitivity analysis of the local Nusselt number distribution with variations Ha and gape between the obstacles.

A consistent feature across both Figs. 7(a) and 7(b) is the undulating profile of the local Nusselt number curves, characterized by distinct peaks. These peaks are consistently located where the fluid directly interacts with the hot surfaces of the internal obstacles, indicating regions of maximized heat transfer. This maximization occurs due to the highest local temperature gradients at these solid-fluid interfaces. The behavior of Nu_x demonstrates a marked sensitivity to both the orientation and the strength of the applied magnetic field.

A fascinating and often non-monotonic trend emerges as the magnetic field angle α is varied. In Fig. 7(a) (Ha = 25) and Fig. 3(b) (Ha = 50), a magnetic field angle of α = 90° (cyan curve) consistently yields the highest local Nusselt number, particularly in the central region of the channel. This seemingly counter-intuitive result, considering that a perpendicular field often maximizes flow suppression, can be attributed to the complex reorientation of flow patterns and the potential induction of beneficial secondary flows or localized recirculation zones. While the overall flow may be damped, the perpendicular Lorentz force can redistribute the fluid in a manner that locally thins the thermal boundary layer adjacent to the heated obstacles, thereby enhancing localized heat transfer.

Conversely, an angle of α = 60° (red curve) often results in the lowest Nusselt number across a significant portion of the channel, particularly between the two main peaks. At this angle, the Lorentz force might not only impede the main flow but also create less favorable flow structures or thicker thermal boundary layers due to reduced effective convection, leading to suboptimal heat transfer. Intermediate angles like α = 0° (blue curve), where the magnetic field is parallel to the primary flow, generally allow for relatively robust convection as the Lorentz force's retarding effect on the main flow is minimal, leading to higher Nusselt numbers than α = 60°. However, they may not achieve the localized enhancements seen at α = 90°. An angle of α = 30° (green curve) shows intermediate performance. This indicates that the optimal angle for heat transfer is highly sensitive to the complex interplay between the magnetic field's direction, fluid properties, and the cavity's geometric configuration.

Comparing Fig. 7(a) (Ha = 25) with Fig. 4(b) (Ha = 50) clearly demonstrates the dominant role of the Ha. As Ha increases from 25 to 50, a general reduction in the local Nusselt number is observed across most angles and locations, particularly in the main flow regions. This decrease is a direct consequence of the intensified Lorentz force at higher Ha. A stronger magnetic field more aggressively impedes the fluid's momentum, leading to a more pronounced suppression of fluid velocity. This increased magnetic braking directly reduces the intensity of convective mixing and heat transport away from the hot surfaces. The slower, more damped flow results in a thicker thermal boundary layer adjacent to the heated obstacles. Since the Nusselt number is inversely related to the boundary layer thickness, its reduction at higher Ha is a direct physical consequence of the intensified magnetic drag, which hinders efficient heat convection. While α = 90° remains the best performer, its peak value still decreases significantly from Ha = 25 to Ha = 50, underscoring the overall detrimental effect of a stronger magnetic field on convective heat transfer. This complex interplay between flow suppression and potential flow restructuring due to the Lorentz force is central to these observations.

Figures 8(a) and 8(b), illustrate the local Nusselt number (Nu_x) variation along the vertical midline (x = 0.5 m) as a function of (Ha) and the gap size (*gp*). In both panels, the magnetic field angle is fixed at α = 90° and Re = 100, while the shape factor is n = 5.7.

A clear trend emerges as Ha increases: for a given gap size, the local Nusselt number generally decreases. In Fig. 8(a) (*gp* = 0.4), the Nu_x values are significantly higher at Ha = 1 (blue curve) compared to Ha = 25 (green curve) and Ha = 50 (red curve). The drop is particularly pronounced at Ha = 50. Similarly, in Fig. 8(b) (gp = 0.6), increasing Ha from 1 to 50 also leads to a substantial reduction in Nu_x. This behavior is attributed to the Lorentz force. A stronger magnetic field (higher Ha) exerts a greater resistive force on the conducting nanofluid, significantly damping its velocity. This suppression of fluid motion reduces convective mixing, thickens the thermal boundary layer, and consequently diminishes the heat transfer efficiency.

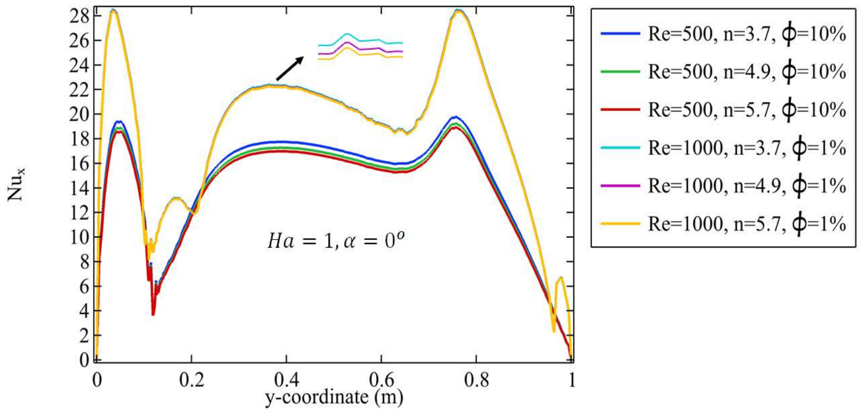

Fig. 9. Sensitivity analysis of the local Nusselt number with the variation of Re, shape factor and the total volume fraction of THNF.

The interplay with the gap size is also evident. Comparing Fig. 8(a) (gp = 0.4) with Fig. 8(b) (gp = 0.6), it is generally observed that a smaller gap leads to higher Nusselt numbers, especially at lower Ha. For instance, at Ha = 1, Nu_x values are noticeably higher for gp = 0.4 than for gp = 0.6. A smaller gap creates a more constricted flow path, forcing the fluid to accelerate and leading to more vigorous convection and thinner thermal boundary layers, thus enhancing heat transfer. However, as Ha increases, the magnetic damping effect becomes dominant, mitigating some of the benefits gained from a smaller gap.

Figure 9 clearly illustrates the sensitivity of the local Nusselt number (Nu_x) along the channel's vertical midline (x = 0.5 (m)) to variations in both the nanoparticle shape factor (n) and the total volume fraction (ϕ) of the THNF. The analysis is conducted under specific fixed conditions of Ha (Ha = 1), magnetic field angle (α = 0°), and two distinct Re (Re = 500 and Re = 1000).

A consistent pattern across all curves is the two-peak profile of Nu_x, which signifies enhanced heat transfer efficiency directly at the hot obstacle surfaces where temperature gradients are steepest. Figure 9 demonstrates that increasing the nanoparticle shape factor (n) generally leads to a decrease in the local Nusselt number. For instance, at Re = 500 and ϕ = 10%, the blue curve (n = 3.7) consistently shows higher Nu_x values compared to the green (n = 4.9) and red (n = 5.7) curves. This is physically attributed to the fact that nanoparticles with more complex or higher shape factors tend to significantly increase the effective viscosity of the nanofluid. This increased viscosity impedes fluid flow and reduces convective mixing, consequently hindering the overall heat transfer process by thickening the thermal boundary layer.

The total volume fraction of the THNF exhibits a strong positive correlation with heat transfer. For a constant Re and shape factor, an increase in ϕ results in a notable increase in the local Nusselt number. This is prominently observed by comparing the sets of curves in Fig. 9: the curves for Re = 1000 and ϕ = 1% show significantly higher Nu_x values than those for Re = 500 and ϕ = 10% (blue, green, red). This enhancement is primarily due to the augmented effective thermal conductivity of the nanofluid as more nanoparticles are introduced. A higher thermal conductivity facilitates more efficient conduction of heat from the hot surfaces into the fluid, thereby boosting the local Nusselt number and improving heat transfer.

Table 4 presents the top 20 parameter estimations that yield the minimum average entropy generation. Conversely, Table 5 lists the top 20 parameter estimations for the minimum average Nusselt number. These tables are generated from an optimization process using the COMSOL Multiphysics with the usage of the Excel, seeking to identify optimal operating conditions.

For minimum average entropy generation (Table 4), the results predominantly show a high Re (Re = 2000) and a lower Hartmann number (Ha = 25). The magnetic field angle (α) varies, with 60° and 90° being common, and a relatively low volume fraction (ϕ = 1%). A common gap size is gp = 0.6, and the shape factor (n) varies. The advantage of minimizing entropy generation is to improve the thermodynamic efficiency of the system, reducing irreversible energy losses due to heat transfer, fluid friction, and magnetic effects. This is crucial for sustainable and energy-efficient designs.

Table 4. Top 20 Parameter Estimations for Minimum Average Entropy Generation along the vertical wall.

Re	Ha	α	ϕ	gp	n	S_{tot}^{avg}
2000	25	60°	1%	0.6	3.7	5.64E-04
2000	25	60°	1%	0.6	4.9	5.72E-04
2000	25	30°	1%	0.6	3.7	5.74E-04
2000	25	60°	1%	0.6	5.7	5.77E-04
2000	25	90°	1%	0.6	3.7	5.80E-04
2000	25	30°	1%	0.6	4.9	5.81E-04
2000	50	90°	1%	0.6	3.7	5.83E-04
2000	25	30°	1%	0.6	5.7	5.86E-04
2000	25	90°	1%	0.6	4.9	5.88E-04
2000	50	90°	1%	0.6	4.9	5.90E-04
2000	25	90°	1%	0.6	5.7	5.93E-04
2000	50	90°	1%	0.6	5.7	5.95E-04
2000	50	60°	1%	0.6	3.7	6.08E-04
2000	50	60°	1%	0.6	4.9	6.15E-04
2000	50	60°	1%	0.6	5.7	6.20E-04
2000	50	90°	0.04%	0.6	3.7	6.43E-04
1000	25	90°	1%	0.6	3.7	6.51E-04
1000	25	90°	1%	0.6	4.9	6.62E-04
2000	25	0	1%	0.6	3.7	6.64E-04
1000	25	90°	1%	0.6	5.7	6.68E-04

Table 5. Top 20 Parameter Estimations for Minimum Average Nusselt number along the vertical wall.

Re	Ha	α	ϕ	gp	n	N_{avg}
100	50	90°	10%	0.6	5.7	17.677
100	50	60°	10%	0.6	5.7	17.677
100	25	60°	10%	0.6	5.7	17.677
100	50	0°	10%	0.6	5.7	17.677
100	25	90°	10%	0.6	5.7	17.677
100	50	30°	10%	0.6	5.7	17.677
100	50	90°	10%	0.4	5.7	17.677
100	25	0°	10%	0.6	5.7	17.677
100	50	60°	10%	0.4	5.7	17.677
100	1	60°	10%	0.6	5.7	17.677
100	1	90°	10%	0.6	5.7	17.677
100	1	30°	10%	0.6	5.7	17.677
100	1	0°	10%	0.6	5.7	17.677
100	50	0°	10%	0.4	5.7	17.677
100	25	30°	10%	0.6	5.7	17.677
100	25	0°	10%	0.4	5.7	17.677
100	50	30°	10%	0.4	5.7	17.677
100	25	30°	10%	0.4	5.7	17.677
100	25	60°	10%	0.4	5.7	17.677
100	50	30°	10%	0.2	5.7	17.677

In contrast, for minimum average Nusselt number (Table 5), the results consistently point towards a low Re (Re = 100) and a higher Hartmann number (Ha = 50). The volume fraction is significantly higher (ϕ = 10%), and the magnetic field angle varies more widely, including 0°-90°. A relatively large gap size (gp = 0.6 or 0.4) is also common. Minimizing the Nusselt number implies minimizing heat transfer. While this might seem counterintuitive for cooling applications, it is advantageous in scenarios requiring thermal insulation or preventing heat loss from a system, such as in certain energy storage devices or medical applications where maintaining a stable temperature is critical. In summary, the tables highlight the trade-offs in design. Achieving high thermal efficiency (low entropy generation) generally requires high Re and lower magnetic effects, whereas minimizing heat transfer necessitates lower Re and stronger magnetic damping.

4.3. Practical and industrial applications of findings

The research on the thermal and fluid dynamic response of a ventilated cavity with two heated obstacles involving advanced ternary nanofluids has vast industrial and practical implications; especially in the realm where thermal management is considered. This research tends to tackle the important problem of improving heat transfer performance, which is an area of concern in modern engineering applications.

One of the more direct applications will be in electronic cooling systems. In line with the trend of making electronic components (i.e., CPUs, GPUs and power electronics) smaller and more powerful, thermal management is critical. The findings of this research, that have analyzed the use of THNF and (MHD) processes to assist with may provide further insights into designing future microfluidic heat sinks and electronic cooling systems. The ability to manipulate a flow field and temperature fields through external magnetic fields is non-interference-based mode of enhancing cooling which has merit for themselves, especially in compact high performance computing systems and data centers.

Beyond electronics, the principles outlined have applicability in the design of medical diagnostics systems. Many of the lab-on-a-chip and microfluidic devices common in point-of-care diagnostics and medical research need accurate temperature control to provide accurate results. There's a lot of interesting research that has been conducted on advanced nanofluids in a ventilated cavity, which provides insight into maintaining consistent thermal conditions in these highly complicated micro-scale systems to ensure that tests are reliable.

5. Conclusion

An electromagnetic effect, set at a directional angle (α), has been utilized for fluid flow and heat transfer within a ventilated cavity containing two hot obstacles. This system features the flow passage of advanced THNF. The numerical solution was generated using COMSOL Multiphysics with a fine mesh density. Six parameters, Reynolds number, Hartmann number, magnetic field angle, nanoparticle shape factor, gap between the hot obstacles, and total volume fraction, were used to analyze the velocity distribution of the domain and the local Nusselt number along the vertical line. The study successfully established the following main points:

- The study's findings indicate that as Ha increases, fluid velocity consequently declines significantly. This is a direct physical outcome of the Lorentz force acting as a resistive magnetic braking force on the electrically conducting fluid, decreasing the fluid's kinetic energy and suppressing fluid circulation, therefore reducing convective heat transfer.
- The physical geometry of the system - specifically, the gap between the obstacles - significantly affected the flow kinematics. A narrower gap restricts flow, yielding a rapid fluid acceleration that produces maximum peak velocities. A narrower gap also enhanced the location of the recirculation zones and vortices formed downstream separated from the obstacle. A wider gap would allow more diffusion of velocity from the obstacle to the field, producing a lower peak velocity and with less instabilities while producing a more stable flow.
- As Re increases, the dominance of inertial forces over viscous forces becomes more apparent. Physically, this is manifested by a direct correlation with higher fluid velocities and stronger, more vigorous circulation patterns within the cavity. This heightened fluid movement is crucial for efficient heat transport.
- Higher Re and increased total volume fractions of nanoparticles lead to a significant increase in the local Nusselt number, indicating enhanced convective heat transfer. Conversely, increasing the Ha or the nanoparticle shape factor generally reduces the local Nusselt number due to increased flow resistance and viscosity, respectively
- A smaller gap between obstacles generally promotes higher local Nusselt numbers by forcing fluid acceleration and intensifying convection, while a wider gap results in lower local Nusselt numbers due to reduced flow constriction.

- The magnetic field angle significantly impacts the local Nusselt number; while increasing Ha generally reduces heat transfer, a perpendicular magnetic field (90°) can lead to localized Nusselt number enhancements, suggesting complex flow restructuring that benefits heat transfer in specific regions.
- Achieving minimum average entropy generation (maximizing thermodynamic efficiency) is predominantly associated with a high Re (Re = 2000), a lower Hartmann number (Ha = 25), a low volume fraction (ϕ = 1%), and a larger gap (gp = 0.6). The magnetic field angle varies but commonly includes 60° and 90° (Table 4).
- Minimizing average Nusselt number (minimizing heat transfer, useful for insulation) is primarily achieved with a low Re (Re = 100), a higher Hartmann number (Ha = 50), a significantly higher volume fraction (ϕ = 10%), and a relatively large gap (gp = 0.4 or 0.6). The magnetic field angle shows wider variation in these optimal conditions (Table 5).

Limitation of the Work and Future Direction: This study on the fluid flow and heat transfer within a ventilated cavity with two obstacles is subject to the assumptions outlined at the end of Section 2.2. To expand upon this research, several avenues for future work are proposed. The phenomenon can be extended by incorporating more advanced nanofluids, such as bi-quadratic nanofluids. Furthermore, different combinations of the three nanoparticles could be explored, and the optimal ratio for mixing the volume fractions could be tested to further enhance the results for temperature and the Nusselt number. The current study is limited to laminar fluid flow. To achieve greater heat transfer, the impact of turbulence, which becomes significant at higher Re, should be investigated. The inclusion of a turbulence model, such as the kappa-epsilon model, would provide a more comprehensive understanding of the system's behavior. Additionally, the impact of a wider range of nanoparticle shape factors should be considered in future work to better optimize heat transfer enhancement. Finally, the angle of the magnetic field was found to be a crucial parameter for visualizing the patterns of the Nusselt number and temperature distribution. Future studies could explore the effects of more specialized angles beyond the well-known ones to uncover new insights into the system's thermal performance.

Author Contributions

A. Phulpoto and A.A. Memon planned the scheme, initiated the project, and did writing and editing of the manuscript; M.A. Memon worked through software and did the formal analysis; K. Jacob developed the mathematical modeling and examined the theory validation. M. Komiljon also provided critical feedback and assisted in revising the manuscript's updated version. All authors discussed the results, reviewed, and approved the final version of the manuscript.

Acknowledgments

The authors extend their profound gratitude to Sukkur IBA University for fostering an exceptionally conducive environment that supports and encourages research publications.

Conflict of Interest

The authors declared no potential conflicts of interest concerning the research, authorship, and publication of this article.

Funding

The authors received no financial support for the research, authorship, and publication of this article.

Data Availability Statements

No data were utilized to perform this research.

Nomenclature

MHD	Magnetohydrodynamics	Gr	Grashof Number
THNF	Ternary Hybrid Nanofluid	GFEM	Generalized Finite Element Method
Re	Reynolds number	PDEs	Partial Differential Equations
Ha	Hartmann number	STHE	Shell-and-tube heat exchanger
PV/T	Photovoltaic Thermal	PARDISO	Parallel Array and Residual-based Distribution Iterative Solution Orchestration
FDLBM	Finite Difference Lattice Boltzmann Method	BFDM	Brinkman-Forchheimer-extended Darcy model

References

[1] Priam, S.S., Saha, R., Saha, S., Pure mixed convection inside a vented square cavity with an isothermally heated rotating cylinder, *AIP Conference Proceedings*, 2324(1), 2021, 050035.

[2] Abu-Hijleh, A.K., Optimized use of baffles for reduced natural convection heat transfer from a horizontal cylinder, *International Journal of Thermal Sciences*, 42(11), 2003, 1061-1071.

[3] Abraham, J.P., Sparrow, E.M., Experiments on discretely heated, vented/unvented enclosures for various radiation surface characteristics of the thermal load, enclosure temperature sensor, and enclosure walls, *International Journal of Heat and Mass Transfer*, 45(11), 2002, 2255-2263.

[4] Saha, S., Islam, M.T., Ali, M., Mamun, M.A.H., Islam, M.Q., Effect of inlet and outlet locations on transverse mixed convection inside a vented enclosure, *Journal of Mechanical Engineering*, 36, 2006, 27-37.

[5] Joodi, A.S., Effect of baffles geometry of the flocculation basin on the turbulence behavior using Comsol multiphysics technique, *Journal of Environmental Studies*, 10(1), 2013, 71-77.

[6] Radhakrishnan, T.V., Joseph, G., Balaji, C., Venkateshan, S.P., Effect of baffle on convective heat transfer from a heat generating element in a ventilated cavity, *Heat and Mass Transfer*, 45(8), 2009, 1069-1082.

[7] Nougbléga, Y., Sagna, K., Atchonouglo, K., Numerical Study of Mixed Convection in Baffled Vented Cavity, *International Journal of Physics*, 8(1), 2020, 1-10.

[8] Mahmood, R., Rehman, N., Majeed, A.H., Rehman, K.U., Shatanawi, W., Numerical solution for heat transfer in a staggered enclosure with wavy insulated baffles, *AIMS Mathematics*, 8(4), 2023, 8332-8348.

[9] Aun, S.H.A., Ghadhban, S.A., Jehhef, K.A., Experimental and numerical investigation of convection heat transfer in an enclosure with a vertical heated block and baffles, *Journal of Thermal Engineering*, 7(3), 2021, 367-386.

[10] Hamzah, H.K., Al-Amir, Q.R.A., Abdulkadhim, A., et al., In a Vented Square Enclosure, the Effect of a Flexible Baffle Attached to a Solid Cylinder on Mixed Convection, *Arabian Journal for Science and Engineering*, 47, 2022, 15489–15504.

[11] Rehman, N., Mahmood, R., Majeed, A.H., et al., Multigrid simulations of non-Newtonian fluid flow and heat transfer in a ventilated square cavity with mixed convection and baffles, *Scientific Reports*, 14, 2024, 6694.

[12] Kefayati, G.R., Mesoscopic simulation of mixed convection on non-Newtonian nanofluids in a two-sided lid-driven enclosure, *Advanced Powder Technology*, 26(2), 2015, 576-588.
[13] Mahmoudi, A.H., Shahi, M., Talebi, F., Effect of inlet and outlet location on the mixed convective cooling inside the ventilated cavity subjected to an external nanofluid, *International Communications in Heat and Mass Transfer*, 37(8), 2010, 1158-1173.
[14] Bellahcene, L., Sahel, D., Yousfi, A., Numerical study of shell and tube heat exchanger performance enhancement using nanofluids and baffling technique, *Journal of Advanced Research in Fluid Mechanics and Thermal Sciences*, 80(2), 2021, 42-55.
[15] Ali, M.M., Akhter, R., Miah, M.M., Hydromagnetic mixed convective flow in a horizontal channel equipped with Cu-water nanofluid and alternated baffles, *International Journal of Thermofluids*, 12, 2021, 100118.
[16] Biswas, N., Mahapatra, P.S., Manna, N.K., Mixed convection heat transfer in a grooved channel with injection, *Numerical Heat Transfer, Part A: Applications*, 68(6), 2015, 663-685.
[17] Biswas, N., Mahapatra, P.S., Manna, N.K., Thermal management of heating element in a ventilated enclosure, *International Communications in Heat and Mass Transfer*, 66, 2015, 84-92.
[18] Biswas, N., Manna, N.K., Datta, P., Mahapatra, P.S., Analysis of heat transfer and pumping power for bottom-heated porous cavity saturated with Cu-water nanofluid, *Powder Technology*, 326, 2018, 356-369.
[19] Barik, A.M., Al-Farhany, K., Numerical Investigation of the Effect of Baffle Inclination Angle on Nanofluid Natural Convection Heat Transfer in A Square Enclosure, *Al-Qadisiyah Journal for Engineering Sciences*, 12(2), 2019, 61-71.
[20] Kumar, S., Gangawane, K.M., Oztop, H.F., A numerical study of mixed convection in a two-sided lid-driven tall cavity containing a heated triangular block for non-Newtonian power-law fluids, *Heat Transfer*, 50(5), 2021, 4806-4829.
[21] Rehman, N., Mahmood, R., Majeed, A.H., Rehman, K.U., Shatanawi, W., Finite element analysis on entropy generation in MHD Iron (III) Oxide-Water nanofluid equipped in partially heated fillet cavity, *Journal of Magnetism and Magnetic Materials*, 565, 2023, 170269.
[22] Mahmood, R., Khan, Y., Rahman, N., Majeed, A.H., Alameer, A., Faraz, N., Numerical computations of entropy generation and MHD ferrofluid filled in a closed wavy configuration: finite element based study, *Frontiers in Physics*, 10, 2022, 916394.
[23] Khan, M.S., Wang, J., Memon, A.A., Muhammad, T., Investigating the enhanced cooling performance of ternary hybrid nanofluids in a three-dimensional annulus-type photovoltaic thermal system for sustainable energy efficiency, *Case Studies in Thermal Engineering*, 60, 2024, 104700.
[24] Galal, A.M., Benabdallah, F., Bayz, D.A., Ching, D.L.C., Memon, A.A., Abbas, M., Khan, I., Said, Y., Effect of thermal radiation on Marangoni convective flow of ternary hybrid nanofluid with bioconvection and local thermal non-equilibrium effects, *Journal of Radiation Research and Applied Sciences*, 18(2), 2025, 101378.
[25] Xia, Z., Wang, J., Memon, A.A., Muhammad, T., Numerical study of heat transfer in a 3D triangular prism with a rotating cylinder using ternary hybrid nanofluids and a new regression model, *Nonlinear Dynamics*, 113(8), 2025, 8161-8192.
[26] Alammari, M., Shaikh, G.M., Memon, A.A., El-Ghareeb, T.H., Fenta, A., Numerical analysis on performance evaluation of photovoltaic thermal systems using ternary hybrid nanofluids and forced convection around copper cylinders, *Results in Engineering*, 24, 2024, 103139.
[27] Rehman, N., Mahmood, R., Majeed, A.H., Khan, I., Mohamed, A., Multigrid simulations of non-Newtonian fluid flow and heat transfer in a ventilated square cavity with mixed convection and baffles, *Scientific Reports*, 14(1), 2024, 6694.
[28] Majeed, A.H., Mahmood, R., Liu, D., Zhang, Y., Zhang, J.Y., Ren, H.Y., Hendy, A.S., Ali, M.R., Effects of oscillation on convective thermal flow in a vertical enclosure filled by nanofluid particles, *Case Studies in Thermal Engineering*, 61, 2024, 105133.
[29] Ullah, S., Saddiq, G., Majeed, A.H., Alotaibi, H., Hendy, A.S., Ali, M.R., Computational study of conjugate heat transfer and entropy generation of hybrid nano-particles in an enclosure with solid block, *Case Studies in Thermal Engineering*, 67, 2025, 105822.
[30] Alqurashi, M.S., Gul, H., Ahmad, I., Majeed, A.H., Khalifa, H.A.E.W., A study of thermal conductivity enhancement in magnetic blood flow: applications of medical engineering, *International Journal of Heat and Fluid Flow*, 112, 2025, 109719.
[31] Majeed, A.H., Mahmood, R., Liu, D., Ali, M.R., Hendy, A.S., Zhao, B., Sajjad, H., Flow and heat transfer analysis over a pair of heated bluff bodies in a channel: characteristics of non-linear rheological models, *Case Studies in Thermal Engineering*, 53, 2024, 103827.
[32] Khan, A., ul Karim, F., Khan, I., Ali, F., Khan, D., Irreversibility analysis in unsteady flow over a vertical plate with arbitrary wall shear stress and ramped wall temperature, *Results in Physics*, 8, 2018, 1283-1290.
[33] Khan, D., Rahman, A.U., Ali, G., Kumam, P., Kaewkhao, A., Khan, I., The Effect of Wall Shear Stress on Two Phase Fluctuating Flow of Dusty Fluids by Using Light Hill Technique, *Water*, 13(11), 2021, 1587.
[34] Rehman, A., Khan, D., Jan, R., Aloqaily, A., Mlaiki, N., Scientific exploring of Marangoni convection in stagnation point flow of blood-based carbon nanotubes nanofluid over an unsteady stretching surface, *International Journal of Thermofluids*, 20, 2023, 100470.
[35] Khan, A., ul Karim, F., Khan, I., Alkanhal, T.A., Ali, F., Khan, D., Nisar, K.S., Entropy generation in MHD conjugate flow with wall shear stress over an infinite plate: exact analysis, *Entropy*, 21(4), 2019, 359.
[36] Elsherbiny, M.S., Ali, M., Shahin, M., El-Kady, M., A review of miniature channels and nanofluids technologies used as heat transfer enhancement techniques for microcooling systems, *Journal of Al-Azhar University Engineering Sector*, 19(72), 2024, 185-211.
[37] Elsherbiny, M.S., Ali, M., Shahin, M., El-Kady, M., Experimental study on the effect of micro concentrations of hybrid nanofluids through microchannel heat sinks, *Journal of Applied and Computational Mechanics*, 11(2), 2025, 303-326.
[38] Alfannakh, H., Numerical analysis of magnetohydrodynamic convection in an inclined cavity with three fins and a ternary composition of nanoparticles, *Processes*, 12(12), 2024, 2889.
[39] Shah, R.K., Thermal entry length solutions for the circular tube and parallel plates, *Proceedings of 3rd National Heat and Mass Transfer Conference*, 1, 1975, 11-75.
[40] Borode, A., Tshephe, T., Olubambi, P., Sharifpur, M., Meyer, J., Stability and Thermophysical Properties of GNP-Fe2O3 Hybrid Nanofluid: Effect of Volume Fraction and Temperature, *Nanomaterials*, 13(7), 2023, 1238.
[41] Mishra, A., Pathak, G., A comparative analysis of MoS2-SiO2/H2O hybrid nanofluid and MoS2-SiO2-GO/H2O ternary hybrid nanofluid over an inclined cylinder with heat generation/absorption, *Numerical Heat Transfer, Part A: Applications*, 85(16), 2024, 2724-2753.
[42] Bawazeer, S.A., Alsoufi, M.S., Natural convection in a square cavity: effects of Rayleigh and Prandtl numbers on heat transfer and flow patterns, *Case Studies in Thermal Engineering*, 73, 2025, 106680.
[43] Bejan, A., Second-law analysis in heat transfer and thermal design, *Advances in Heat Transfer*, 15, 1982, 1-58.
[44] Mahmud, S., Fraser, R.A., Flow, thermal, and entropy generation characteristics inside a porous channel with viscous dissipation, *International Journal of Thermal Sciences*, 44(1), 2005, 21-32.

ORCID iD

Abid A. Memon https://orcid.org/0000-0002-3114-8062
M. Asif Memon https://orcid.org/0000-0002-2608-6557
Kavikumar Jacob https://orcid.org/0000-0002-2314-4600

How to cite this article: Phulpoto A., et al., Finite Element Analysis of MHD Thermal Management in a Ventilated Cavity with Dual Obstacles Using Advanced Ternary Hybrid Nanofluids, *J. Appl. Comput. Mech.*, 12(3), 2026, 848-865. https://doi.org/10.22055/jacm.2025.48499.5278